nature materials

Article

https://doi.org/10.1038/s41563-025-02234-6

Hybrid hydrogel–extracellular matrix scaffolds identify biochemical and mechanical signatures of cardiac ageing

Received: 7 September 2023

Accepted: 4 April 2025

Published online: 12 June 2025

Check for updates

Avery Rui Sun[1,2], Md Faris H. Ramli[1], Xingyu Shen[1], Karthikbabu Kannivadi Ramakanth[3], Dixiao Chen[1], Yang Hu[4,5], Prasanna Vidyasekar[4,5], Roger S. Foo[4,5], Yuchen Long[1,3], Jin Zhu[1], Matthew Ackers-Johnson[4,5] & Jennifer L. Young[1,2]

Extracellular matrix remodelling of cardiac tissue is a key contributor to age-related cardiovascular disease and dysfunction. Such remodelling is multifaceted including changes to the biochemical composition, architecture and mechanics, clouding our understanding of how and which extracellular matrix properties contribute to a dysfunctional state. Here we describe a decellularized extracellular matrix–synthetic hydrogel hybrid scaffold that independently confers two distinct matrix properties—ligand presentation and stiffness—to cultured cells in vitro, allowing for the identification of their specific roles in cardiac ageing. The hybrid scaffold maintains native matrix composition and organization of young or aged murine cardiac tissue, whereas its mechanical properties can be independently tuned to mimic young or aged tissue stiffness. Seeding these scaffolds with murine primary cardiac fibroblasts, we identify distinct age- and matrix-dependent mechanisms of cardiac fibroblast activation, matrix remodelling and senescence. Importantly, we show that the ligand presentation of a young extracellular matrix can outweigh the profibrotic stiffness cues typically present in an aged extracellular matrix in maintaining or driving cardiac fibroblast quiescence. Ultimately, these tunable scaffolds can enable the discovery of specific extracellular targets to prevent ageing dysfunction and promote rejuvenation.

Age-related alterations in tissue properties have been recognized as key drivers of organ dysfunction and disease. Although much remains unknown about what happens to the extracellular matrix (ECM) at the micro and nano length scales during these large-scale remodelling events, it is widely acknowledged that the mechanics, organization and composition of the ECM vary with age. For instance, it has been shown that the cardiac muscle stiffens[1], whereas ECM composition and organization undergo age-dependent modifications[2–4]. Cardiac fibroblasts (CFs) are the resident cells largely responsible for the remodelling of heart tissue and are known to be mechanosensitive from both in vitro and in vivo studies[5,6].

In healthy tissue, CFs largely remain in a quiescent state, but external stimuli, including biochemical, structural and mechanical cues[5–7], are able to activate quiescent CFs, leading to their differentiation into a proto-myofibroblast phenotype and subsequently into a mature myofibroblast phenotype when these stimuli are impactful and persistent[6,8]. The process of CF activation and proper myofibroblast maturation are essential for ECM deposition and the maintenance of

A full list of affiliations appears at the end of the paper. e-mail: biejly@nus.edu.sg

matrix homeostasis but can also lead to fibrosis and result in functional consequences[9]. This is important in ageing tissues, as alterations in the ECM can be vast and multifaceted, thereby leading to the activation of CFs and subsequent aberrant tissue remodelling[6,10].

Indeed, it has been shown that myofibroblasts are more abundant in aged versus young hearts and directly induce changes to the tissue geometry[10–12]. Although in vitro material systems have identified individual properties of the ECM that play distinct roles in CF function, it remains a challenge to vary these properties independently. In most scaffold platforms, tuning the mechanical properties will alter the ligands and/or architecture. A handful of novel material systems have been described that are capable of independent tunability[13–15], yet the incorporation of native ECM properties is still lacking. Thus, our understanding of the specific contributions stemming from ECM cues is currently limited. We, therefore, sought to develop a native ECM-based scaffold in which we could individually tune the mechanics and faithfully mimic the in vivo cardiac environment—both composition and architecture—allowing for the identification of ECM-specific roles in age-related CF activation, mechanosensing, matrix remodelling and senescence.

To do this, we developed a novel approach called DECellularized In situ Polyacrylamide Hydrogel–ECM hybRid (DECIPHER) that integrates polyacrylamide (PA)-hydrogel-linked cardiac tissue slices and in situ decellularization of ECM. We demonstrate that our decellularization technique is not only able to maintain the ECM composition and fibre architecture but that the samples can be tuned to exhibit young or aged stiffness, namely, ~10 kPa or 40 kPa, respectively. Furthermore, we demonstrate the ability of DECIPHER scaffolds to exhibit physiologically relevant viscoelastic properties due to the interpenetrating network. Seeding young and aged CFs onto combinations of young or aged matrix with young or aged stiffness, we demonstrate distinct age-dependent CF activation, mechanosensing, ligand interaction, ECM remodelling and senescence. Although we observe that such phenotypes can be driven by multiple matrix cues, ECM ligand presentation can outweigh the ECM mechanics, with young ECM promoting CF quiescence despite the profibrotic stiffness cue that is characteristic of aged cardiac tissue. These findings provide a unique insight into the distinct roles of ECM in regulating age-related cardiac dysfunction, which have important implications in matrix-based treatment strategies.

DECIPHER maintains native ECM ligands

The DECIPHER method (Fig. 1a) was inspired by a previously reported method for tissue clearing[16], in which N-methylolacrylamide, formed by prereacting acrylamide hydrogel solution with formaldehyde, binds to the amine groups of tissue proteins. After crosslinking the PA hydrogel with ultraviolet (UV) light, the tissue proteins are stabilized onto the PA mesh, thereby making an interpenetrating and interconnected hybrid hydrogel, and then decellularized in place. We modified the original method in three ways: (1) by linking the PA gel to methacrylated coverslips, enabling stable sample handling; (2) by modifying the PA hydrogel solutions to dictate the scaffold stiffness; and (3) by applying an optimized decellularization method to maintain the ECM composition and architecture.

With DECIPHER, we created four sample combinations of young (1–2 months) and aged (18–24 months) ECM, from isolated native murine tissue sections, and young and aged stiffness, dictated by the hydrogel component; in all these cases, the native tissue architecture was maintained (Fig. 1b). These samples are referred to as follows: 'SoftY' for soft, young ECM; 'StiffY' for stiff, young ECM; 'SoftA' for soft, aged ECM; and 'StiffA' for stiff, aged ECM (Fig. 1 and Extended Data Fig. 1a). Decellularization increases the transparency of the tissue, and the DECIPHER sample is stabilized within the PA hydrogel on a coverslip (Fig. 1c). Scanning electron microscopy (SEM) of the DECIPHER samples show a crosslinked fibrous structure on the ECM due to PA stabilization, which is not present surrounding the collagen fibrils in native tissue (Fig. 1d). Confocal imaging of Nile Blue-tagged acrylamide and collagen (CNA35) reveals the penetration of PA into the tissue and surrounding ECM fibres, leaving the ECM exposed on the surface for cell binding (unmodified PA hydrogels repel cell adhesion[17]) due to the placement on a hydrophobic glass slide at the surface during polymerization (Fig. 1e).

Immunohistochemistry (IHC) of the nuclei and actin in young and aged tissues confirmed the complete removal of cellular structures and the preservation of ECM composition and organization (collagen, fibronectin, hyaluronan and laminin) (Fig. 2a,b). PicoGreen dsDNA assay (Extended Data Fig. 1c) further verified full decellularization[18], whereas collagen and sulfated glycosoaminoglycan (sGAG) quantifications showed minimal loss post-DECIPHER (>95.8% of collagen and >52.0% of sGAG were preserved; Extended Data Fig. 1d,e). The loss of sGAGs was ascribed to their removal on the plasma membrane and inside cells[19]. After optimizing the decellularization approach to be minimally damaging using sodium deoxycholate (SDC) and deoxyribonuclease (DNase), we confirmed that collagen fibrils remained intact through the staining and quantification of collagen hybridizing peptide (Extended Data Fig. 1g,h). We compared our decellularization method with a widely used decellularization protocol (sodium dodecyl sulfate (SDS) + Triton X-100) and found denatured collagen in both PA-stabilized and unstabilized samples (Extended Data Fig. 1g,h), although hydrogel stabilization was effective in reducing collagen denaturation.

We next quantified the ECM architecture from collagen IHC images using the TWOMBLI Fiji plug-in[20]. A principal component analysis shows no difference between the pre- versus post-DECIPHER or soft versus stiff samples across multiple geometric parameters (branch points, fractal dimension, alignment, endpoints, hyphal growth unit and lacunarity) (Fig. 2c,d). Importantly, we quantitatively demonstrate that young versus aged ECM exhibits distinguishable architectural differences across all architectural readouts, where endpoints per unit length (hyphal growth unit) was identified with the greatest principal component contribution (Extended Data Fig. 1f), further emphasizing the importance of ECM architecture in ageing (Fig. 2d).

DECIPHER decouples ECM ligands and stiffness

One of the major improvements that DECIPHER brings to current decellularized ECM (dECM)-based material systems is in situ hydrogel–tissue stabilization. Hydrogel stabilization not only prevents tissue architecture disruption and damage during decellularization but also confers tunable mechanical properties to the scaffold. Using nanoindentation, we first measured the stiffness (Young's modulus E) of the native tissue obtained from young or aged murine hearts (Fig. 2e). Young and aged tissues were found to have $E = 13.1 \pm 5.2$ kPa and 38.6 ± 7.9 kPa, respectively, consistent with previous reports[1]. Subsequently, we optimized the PA hydrogel compositions to mimic the measured tissue stiffnesses, $E = 11.5 \pm 0.9$ kPa and 39.6 ± 4.0 kPa for young and aged tissue stiffnesses, respectively (Fig. 2f). Stiffness mapping of pre- and post-DECIPHER samples was carried out and demonstrated the ability to obtain decoupled stiffness tunability from native tissue stiffness (Fig. 2g and Extended Data Fig. 2a).

We next sought to quantify the viscoelastic properties of the DECIPHER scaffolds. Interpenetrating network materials have been shown to exhibit time-dependent mechanics[14], which is important for biomaterials design due to the inherent viscoelasticity of most tissues, including the heart[21,22]. Plain PA hydrogel recipes used in this study were shown to be purely elastic (Fig. 2h), whereas DECIPHER scaffolds exhibited viscoelastic properties, with loss moduli ranging from ~3.5 kPa to 4.8 kPa for SoftY scaffolds and ~5.4 kPa to 7.3 kPa for StiffY scaffolds (Fig. 2i and Extended Data Fig. 2b,c). These ranges match the reported tissue viscoelasticity values and are an improvement over the reconstituted dECM materials[21], further emphasizing the ability of our scaffolds to mimic native tissue mechanical properties. We also

https://doi.org/10.1038/s41563-025-02234-6

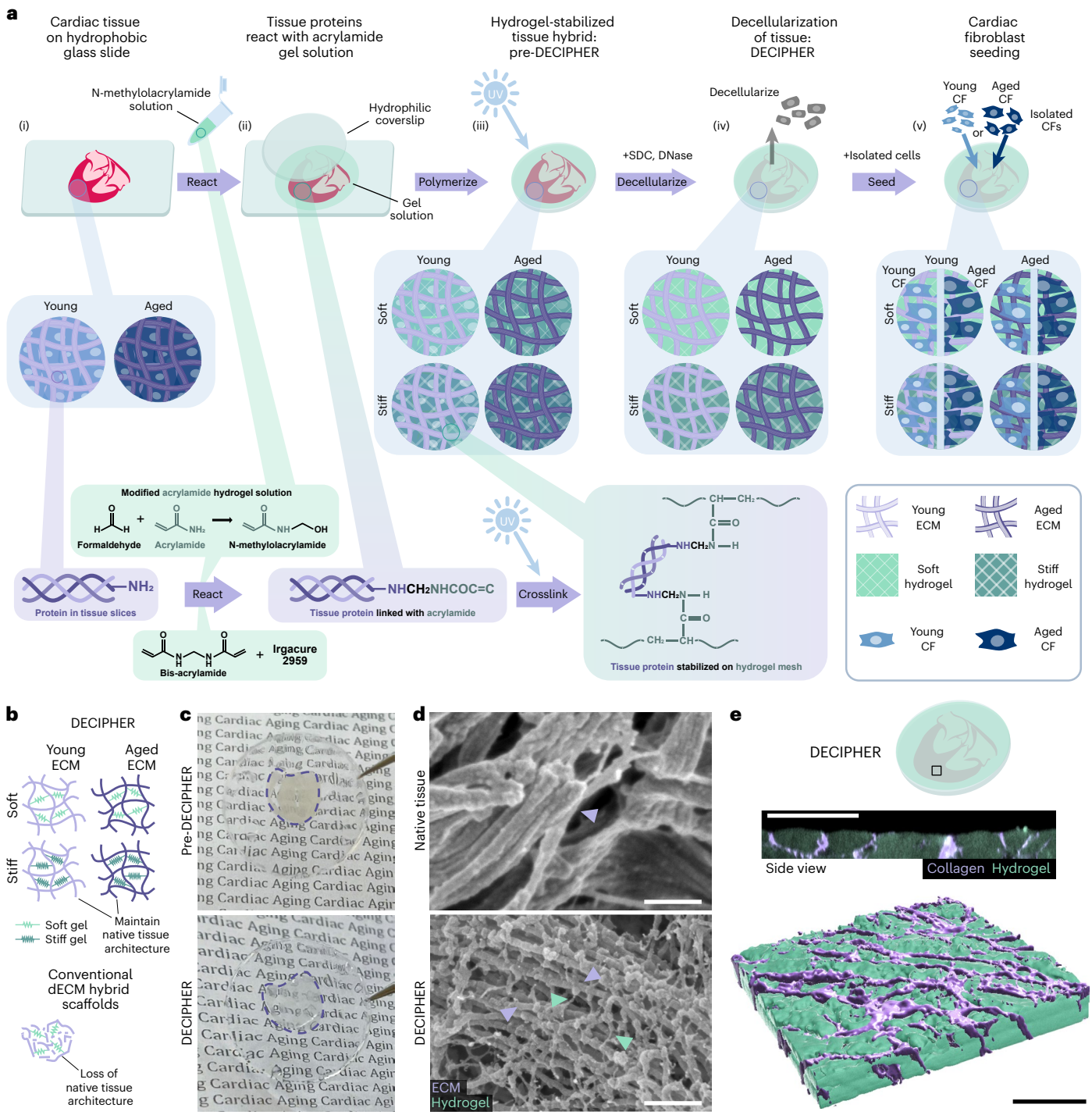

Fig. 1 | The DECIPHER system. a, Murine cardiac tissue (young and aged) was sliced with a vibratome, placed on a hydrophobic glass slide (i) and incubated in a hydrogel stabilization solution consisting of acrylamide pretreated with formaldehyde, bis-acrylamide and Irgacure 2959 of soft (~10 kPa) or stiff (~40 kPa) formulations (ii). Crosslinking of the hydrogel mesh was carried out with UV (iii). At this step, the tissue is stabilized in the hydrogel mesh (as indicated in the box below) and samples are referred to as 'pre-DECIPHER'. Subsequent decellularization is carried out using SDC and DNase (iv) and samples are referred to as 'DECIPHER'. The scaffolds are seeded with young or aged CFs (v). **b**, DECIPHER maintains the native tissue architecture and mechanics, compared with conventional dECM hybrid materials. **c**, Images of pre-DECIPHER and DECIPHER samples with a tissue/ECM scaffold indicated by the dashed lines, surrounded by a coverslip/pure PA gel. **d**, SEM images of native tissue and DECIPHER samples with arrows indicating the ECM fibres versus the hydrogel mesh. Scale bars, 200 nm. **e**, Three-dimensional confocal reconstruction of DECIPHER samples with Nile Blue-tagged acrylamide and labelled collagen. Scale bars, 50 µm.

demonstrate that the covalent linking between the hydrogel and ECM fibres enhances the viscoelastic properties of the scaffolds (Extended Data Fig. 2f,g), and plain PA hydrogel mechanics were not influenced by the linking agent (Extended Data Fig. 2d,e).

The nanoindentation experiments described above use a 50-µm-radius spherical cantilever, which is unable to distinguish nanoscale ECM fibre mechanics. Thus, we sought to map the mechanical properties at higher resolution by applying correlative

https://doi.org/10.1038/s41563-025-02234-6

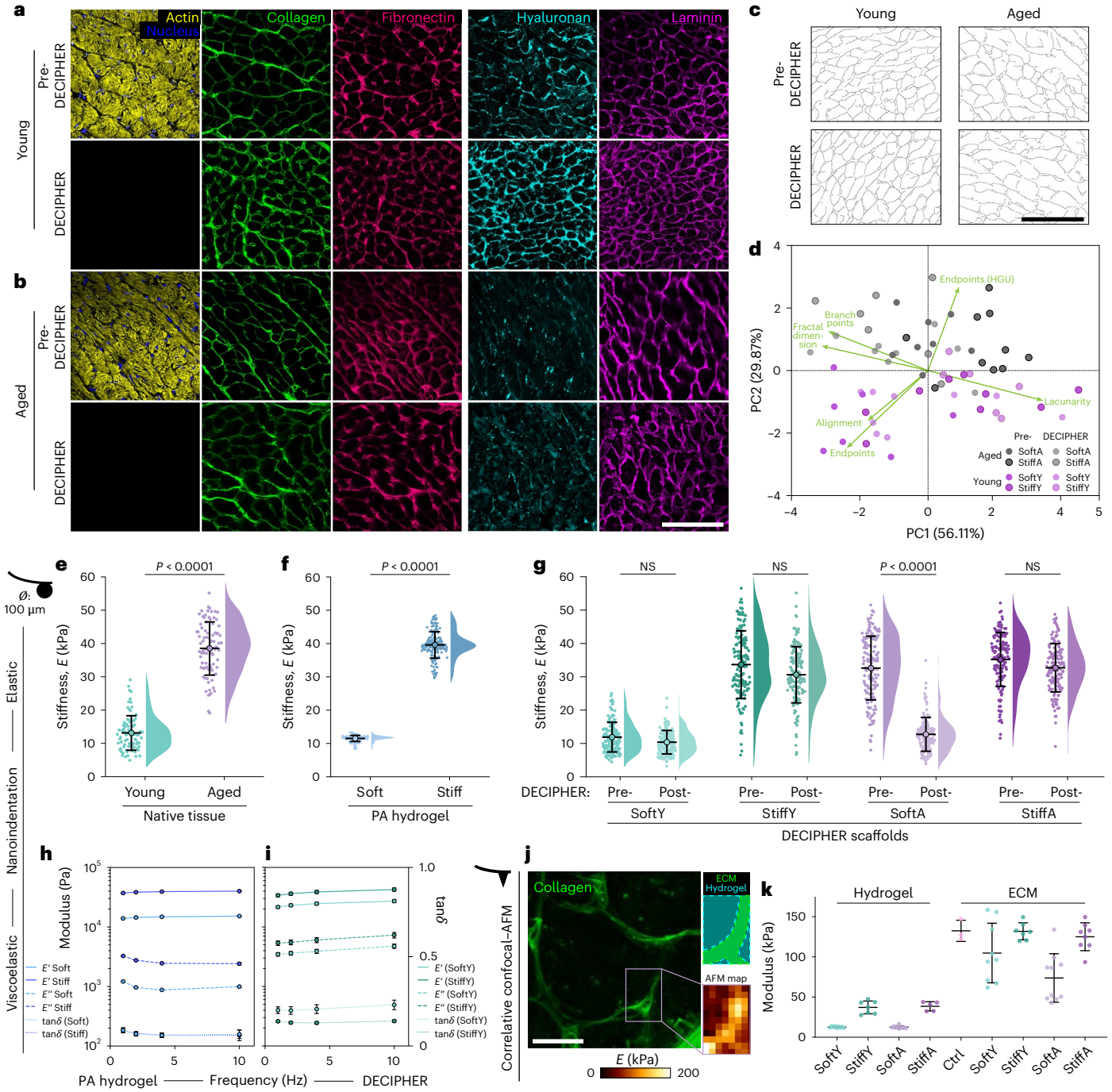

Fig. 2 | DECIPHER preserves ECM with tunable stiffness. a,**b**, IHC of pre-DECIPHER (top set) and DECIPHER (bottom set) samples from young (**a**) and aged (**b**) murine cardiac tissue for nucleus, actin, collagen, fibronectin, hyaluronan and laminin show the removal of cellular structures in DECIPHER versus pre-DECIPHER samples, as well as the preservation of ECM components. **c**,**d**, Collagen architecture of young or aged tissue ($N = 3$ biological replicates for each condition) in pre-DECIPHER and DECIPHER scaffolds were quantified using TWOMBLI (**c**) followed by a principal component analysis (**d**). HGU, hyphal growth unit. **e**,**f**, Nanoindentation of native cardiac tissue from young and aged mice (**e**; $N = 3$ biological replicates for each condition) was used to dictate the PA hydrogel compositions for soft and stiff samples (**f**; Soft ($N = 5$ gels) and Stiff ($N = 7$ gels)). **g**–**i**, Stiffness mapping of DECIPHER samples showed mechanical tunability to maintain stiffness in SoftY, increase stiffness in StiffY, decrease stiffness in SoftA and maintain stiffness in StiffA (**g**; $N = 3$ biological replicates for each condition). Viscoelastic properties were measured using dynamic mechanical analysis for plain PA hydrogel (**h**; $N = 3$ gels) and DECIPHER samples (**i**; $N = 3$ biological replicates for each condition). **j**,**k**, Correlative confocal–AFM was performed on DECIPHER samples for collagen fibres and the surrounding hydrogel (**j** and **k**; $N = 2$ biological replicates for each condition). Data are mean ± s.d. (**e**–**g** and **k**) or mean ± s.e.m. (**h** and **i**). Unpaired two-tailed t-test (**e** and **f**) or one-way analysis of variance (ANOVA) with Dunn's multiple comparisons (**g**). NS, not significant ($P > 0.05$). Scale bars, 100 µm (**a**–**c**); 10 µm (**j**).

confocal–atomic force microscopy (AFM). To do this, we live stained collagen fibres to identify specific regions of interest with confocal microscopy and then moved to the same position in the AFM setup[23]. By scanning the surface of DECIPHER samples with a nanometre-sized pyramidal-shaped cantilever, we found that the DECIPHER process does not impact the ECM fibre stiffness across all the sample conditions compared with the native tissue control samples, although collagen bundle size could contribute to stiffness variance (Fig. 2j,k and

Extended Data Fig. 2h). When measuring the mechanics in regions adjacent to the ECM fibres, we measured the expected values based on the hydrogel formulations used (for example, ~12.6 kPa in SoftY or SoftA gel regions and ~37.8 kPa in StiffY or StiffA gel regions; Fig. 2k). This means that the hydrogel component provides the indentation resistance of the entire hybrid scaffold, as dECM alone has been shown to exhibit reduced compressive modulus and spontaneous shrinkage when unrestrained[24,25]. Taken together, DECIPHER allows for the mechanical tunability of decellularized tissue that is decoupled from native ECM composition and architecture.

Ageing alters intra- and extracellular cardiac phenotypes

CFs are largely responsible for cardiac ECM remodelling[3,26]. To characterize age-related changes in both CFs and ECM of young (1 month) and aged (24 months) mice, we performed RNA sequencing (RNA-seq) on isolated primary CFs and tandem-mass-tag-based quantitative mass spectrometry on dECM from cardiac tissue. For RNA-seq, isolated cells were examined for cell-type-specific markers for *Vim* (encodes vimentin in fibroblasts), *Pecam1* (encodes CD31 in endothelial cells) and *Tnni3* (encodes Troponin I in cardiomyocytes), confirming a pure fibroblast population in both age groups (Extended Data Fig. 3n). Differentially expressed gene (DEG) analysis of aged versus young CFs found 490 upregulated genes and 597 downregulated genes (Fig. 3a), with heat maps showing global differential expression patterns between cell populations (Fig. 3b). Those upregulated included multiple senescence markers (for example, cellular communication network factor 1 (*Ccn1*), *Cdkn1a* and *Cdkn2*) and fibroblast-associated profibrotic markers (for example, *Ankrd1*, *Tnc*, *Ccr2* and *Adamts1*). The majority of significantly downregulated genes encode ECM proteins (for example, *Col1a1, Col1a2, Col3a1*, *Fn1* and *Eln*), which have been observed in aged rodent models[3], as well as matricellular protein gene *Ccn5*, cyclin family genes (for example, *Ccnb1* and *Ccnb2*) and cyclin-dependent kinase-encoding genes (for example, *Cdk1* and *Cdk6*), indicating both increased potential of aged CFs to be activated[27] and abnormal proliferative ability that could suggest a senescent-like phenotype[28,29] (Fig. 3a). KEGG enrichment analysis of the DEGs in aged versus young CFs corroborated these findings as multiple significantly upregulated pathways indicated their greater potential towards profibrotic ECM remodelling, a senescent-like phenotype, and ECM deregulation as found in the aged heart[3] (Fig. 3c).

Quantitative mass spectrometry found more than 3,000 proteins in decellularized young and aged cardiac tissues, with the extracted proteome highly enriched in ECM proteins based on gene ontology enrichment analysis (Extended Data Fig. 1m). Differentially expressed protein (DEP) analysis identified 117 upregulated and 58 downregulated proteins (Fig. 3d,e). Due to a larger CF population and altered ECM turnover in the aged heart[11,12,30], many ECM proteins were found to be significantly upregulated in cardiac ageing (Fig. 3e and Extended Data Fig. 1o) including collagen VI, laminin α2, laminin β2, fibronectin, vitronectin, versican, decorin, periostin, collagen XII and perlecan, whereas elastin, collagen III and aggrecan were found to be downregulated (Extended Data Fig. 1o). Matrix-immobilized molecules were also identified, with greater TGF-βI, CXCL12 and LOXL1 found in aged ECM (Extended Data Fig. 1n). By analysing the protein–protein interaction (PPI) network using the STRING database, we found that structural ECM proteins, matricellular proteins, matrix-immobilized molecules, membrane-associated proteins and other functional proteins are closely associated, with fibronectin, vitronectin and nidogen having the largest contributions (Extended Data Fig. 1p).

We next characterized the ligand–receptor interactome using these two datasets[31]. By comparing the top 20 up- or downregulated extracellular proteins of the ECM with the top 25 lowly or highly expressed cell surface molecules, we can understand the age-specific regulation of matrix-mediated signalling processes[10,32]. We find enhanced integrin expression in aged versus young CFs (for example, genes encoding integrins $\alpha_{v/4/6/9/10}$ and $\beta_{1/3/6}$) corresponds to upregulated ECM components in aged tissue (for example, laminins α2/α4/β1, fibronectin, versican, periostin and perlecan; Fig. 3f). Genes encoding non-integrin receptors were also identified in the top regulated CF receptors with ageing (for example, *Egfr* and *Cd44* are upregulated; *Sdc3* is downregulated) and correlate with ECM abundance.

CF gene expression is regulated by ECM as a function of age

We next sought to understand how young and aged CFs perceive and respond to ECM stiffness and ligands, both individually and cooperatively, using our DECIPHER scaffolds (all combinations are detailed in Extended Data Fig. 1b). We first compare our most aged state (that is, aged CFs cultured on a scaffold representing the aged heart, StiffA) to our most young state (that is, young CFs cultured on a scaffold representing the young heart, SoftY) (Fig. 3g,h). After culturing primary CFs on DECIPHER samples, we identified global DEGs (>1,100 genes) in the aged versus the young state (Fig. 3i). Upregulated genes include those that encode matrix remodellers (for example, *Timp3* and *Lox*), specific ECM proteins (for example, *Col12a1* and *Col8a1*) and activators of fibroblasts (for example, *Ccn4* and *Ccnd2*), whereas downregulated genes include those that encode matrix degraders (for example, *Mmp2* and *Mmp12*), matrix adhesions (for example, *Dpt* and *Itga8*) and specific ECM proteins (for example, *Eln* and *Col13a1*).

When comparing aged CF gene expression on all other DECIPHER samples versus StiffA, the cells exhibited a rejuvenation-like effect, shifting expression towards a quiescent phenotype, particularly on the young ECM samples (Fig. 3j; original clustering data are shown in Extended Data Fig. 4a). The opposite trend was observed for young CFs on all other DECIPHER samples versus SoftY, with the expression indicating an ageing-like shift and enhanced activation (Fig. 3j). Interestingly, ligand presentation had a larger impact compared with stiffness in driving aged cells towards a young state.

We further applied comprehensive pairwise KEGG enrichment analyses on all DECIPHER samples to identify specific pathways that were activated or suppressed by stiffness cues as a function of age (Extended Data Fig. 5a) or by ECM as a function of age (Extended Data Fig. 5b). We found that stiffness activates nucleocytoplasmic transport, whereas ligand presentation promotes arginine and proline metabolism, which regulates collagen synthesis and has been associated with ECM-driven fibrotic remodelling in other tissues[33,34]. In summary, primary aged CFs exhibit both senescent and activated phenotypes, and young ECM is able to shift expression, regardless of stiffness, towards a rejuvenated-like state. Conversely, both higher stiffness and aged ECM can shift young CFs towards a more activated and aged-like state. These matrix-property-specific differences between young and aged CFs underscore the interplay of cellular and extracellular ageing, which DECIPHER is capable of unravelling.

Age regulates ligand interactions and mechanosignalling

Cellular mechanotransduction is triggered after interaction with the ECM; thus, we sorted our RNA-seq data for membrane receptors and well-known mechanosensors (Fig. 4a; Extended Data Figs. 3 and 6 show both RNA-seq and reverse-transcription (RT) quantitative polymerase chain reaction (qPCR)). Overall, young CFs upregulated mechanosensitive gene expression on stiff substrates regardless of the ECM, whereas aged CFs showed mechanosensing impairments, as previously reported[10]. Furthermore, age-specific receptor expression was conserved on DECIPHER samples, correlating with data from freshly isolated cells (Figs. 4a and 3f). Delving deeper into age- and ECM-specific ligand–receptor responses after culturing CFs on DECIPHER samples, we found the expression of *Ddr2* (encoding discoidin domain receptor 2 (DDR2)), which is associated with CF activation and ECM remodelling

https://doi.org/10.1038/s41563-025-02234-6

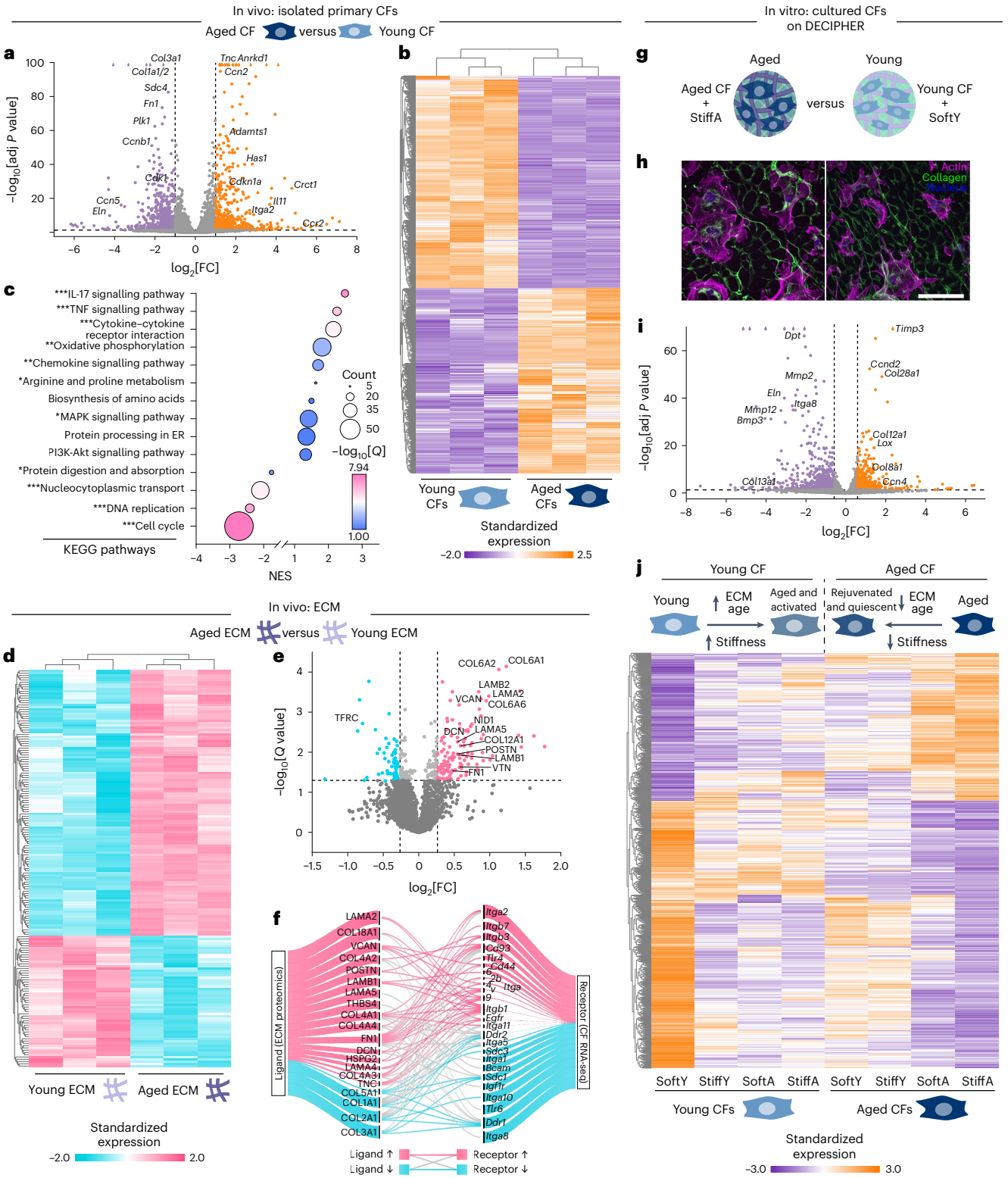

Fig. 3 | Age-dependent regulation and ligand–receptor interactions in CFs and native cardiac ECM. a, DEG analysis of RNA-seq data of primary aged versus young CFs show fold-change (FC) expression, with the specific upregulated and downregulated genes highlighted. **b**, Heat map of clustered DEGs with three sample replicates of young and aged CFs. **c**, KEGG enrichment analysis of aged versus young CF DEGs shows the activated and suppressed pathways. The bubble size indicates the number of DEGs in each pathway set and the colour bar indicates the adjusted significance by *Q* value. Significantly regulated pathways are marked with asterisks on the *y* axis: **Q* < 0.05, ***Q* < 0.01, ****Q* < 0.001. **d**,**e**, DEPs in aged versus young cardiac ECM shown as the clustered heat map (**d**) and volcano plot (**e**), with the upregulated and downregulated expressions indicated. **f**, Ligand–receptor interaction map for the top 25 CF receptors and top 20 ECM ligands, where the bar width indicates the FC expression in aged versus young and node colours indicate the correlation of two ends. **g**–**j**, DECIPHER comparisons of 'aged heart' (aged CFs on StiffA) versus 'young heart' (young CFs on SoftY) (**g** and **h**), with the DEGs shown in the volcano plot (**i**) and heat map (**j**). *N* = 3 biological replicates for each condition, two-sided Benjamini–Hochberg test (**a**–**e**, **i** and **j**). DEGs are FC > 2 and *P* < 0.05 in **a** and **b**; FC > 1.5 and *P* < 0.05 in **i** and **j**; DEPs are FC > 1.2 and *P* < 0.05 in **d**–**f**. The colour bars in **b**, **d** and **j** indicate the row-standardized expression. Scale bar, 100 µm (**h**).

https://doi.org/10.1038/s41563-025-02234-6

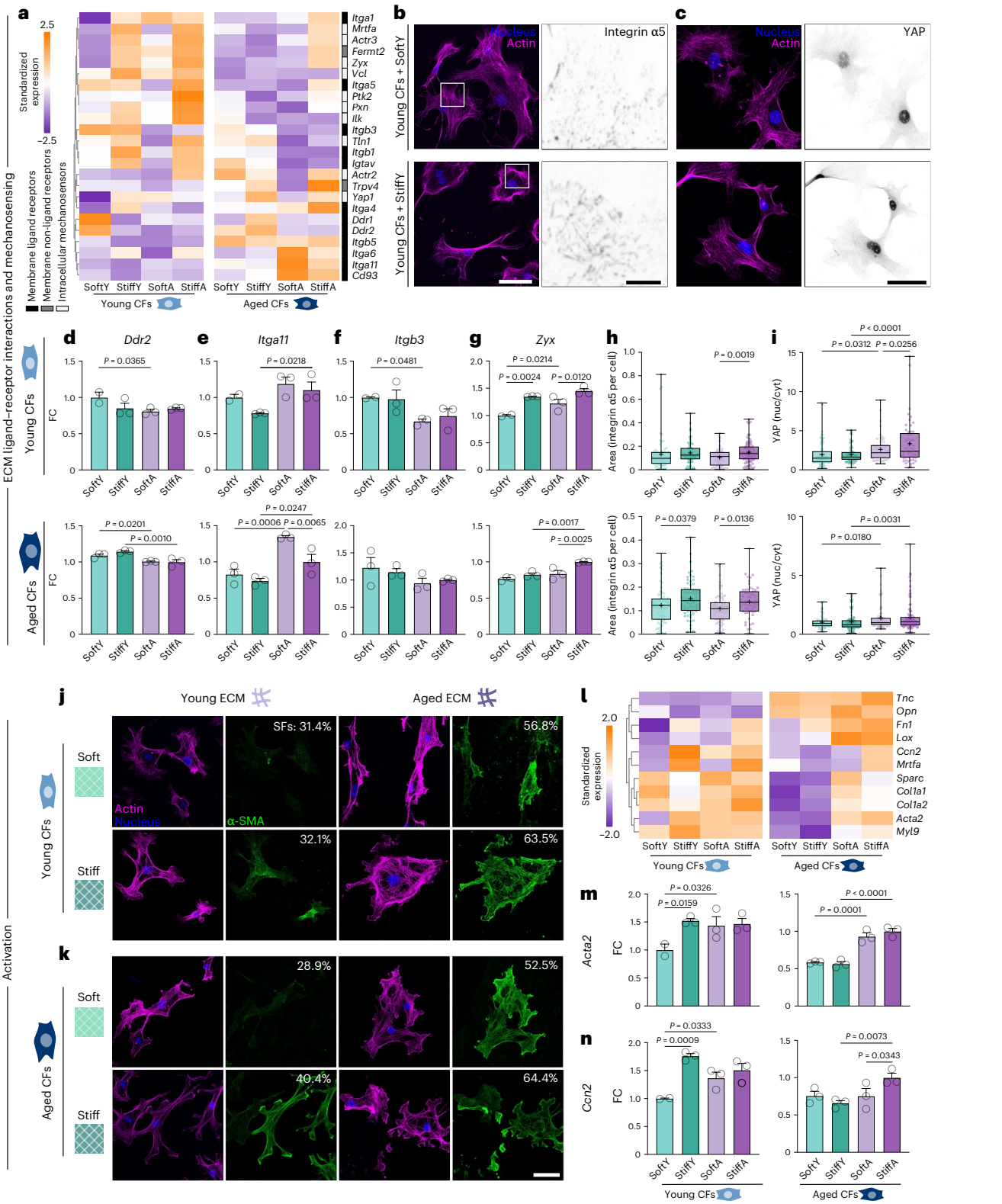

Fig. 4 | ECM ligand cues can override mechanical cues in CF activation and mechanotransduction. a–**n**, RNA-seq data analysis and ICC for ECM ligand–receptor interactions and mechanosensing (**a**–**i**) and activation (**j**–**n**) are shown. **a**, RNA-seq analysis of ECM receptors and mechanosensitive proteins of young and aged CFs on DECIPHER samples. **d**–**g**, Normalized gene expression for highlighted membrane receptors (*Ddr2*, *Itga11* and *Itgb3*) and intracellular mechanosensors (*Zyx*). **b**,**c**,**h**–**k**, Highlighted ICC groups of young CFs on SoftY or StiffY DECIPHER samples stained for nucleus, F-actin and α5 integrin (**b**), YAP (**c**) or α-SMA (**j** and **k**), and quantified in **h** and **i**. SF, stress fibres (**j**). *N* = 3 samples for each condition in each ICC (**b**, **c** and **h**–**k**). **l**, CF activation genes from the RNA-seq data of young and aged CFs on DECIPHER samples. **m**,**n**, Normalized gene expression for CF activation markers (*Acta2* and *Ccn2*) for young and aged CFs on DECIPHER samples. The colour bar indicates the row-standardized expression (**a** and **l**). Data are mean ± s.e.m. (**d**–**g**, **m** and **n**). One-way ANOVA with Fisher's preplanned multiple comparisons (each pair with one variable, ECM or stiffness) was used for **d**–**i**, **m** and **n**. Scale bars, 10 µm (inset of α5 integrin in **b**); 50 µm (**b**, **c**, **j** and **k**).

in the pathological heart[35], to be inversely related to age—young CFs on aged ECM have reduced *Ddr2* expression, whereas aged CFs on young ECM have enhanced expression (Fig. 4d).

Among integrins, α_{11} is an important collagen receptor that modulates CF activation and ECM protein synthesis in disease models, although its mechanosensitive function remains unclear[29,36]. Using DECIPHER, we observed a significant increase in α_{11} integrin expression on aged ECM (Fig. 4e), whereas stiffness did not play a major role. Fibronectin-binding integrins (for example, $\alpha_5\beta_1$ and $\alpha_v\beta_3$) are regulated by age and fibronectin tensional state, which has been shown to alter biochemical and mechanosignalling via focal adhesion recruitment[4]. The immunostaining of α_5 integrin confirmed its mechanosensitive nature[37,38], with larger α_5 clusters on stiff substrates regardless of ECM (Fig. 4b,h and Extended Data Fig. 7a,b). By contrast, RNA-seq shows β_3 integrin gene expression is regulated by ECM age (Fig. 4f), where we observed reduced expression on aged ECM for both young and aged CFs. These results highlight that specific receptors exhibit unique responses to the extracellular environment.

We next focused on intracellular mechanosensors from our RNA-seq data (Fig. 4a). Specifically, young CFs upregulated focal adhesion, serum response factor/myocardin-related transcription factor A (*Mrtfa*) and *Yap1* gene expression on stiff and/or aged substrates (StiffY, SoftA and StiffA). Aged CFs, on the other hand, generally required both aged ECM and high stiffness (StiffA samples) to upregulate mechanosensitive genes. At the focal adhesion level, zyxin (*Zyx*)—responsible for actin regulation—was significantly upregulated in young CFs when exposed to either aged ECM and/or a stiff environment, whereas aged CFs required both cues presented together to increase expression (Fig. 4g). Immunocytochemistry (ICC) staining of focal adhesion sites (paxillin) showed a reduction in their formation on soft and/or young ECM, suggesting a less activated phenotype (Extended Data Fig. 7c–h).

Despite altered mechanosignalling, we found that *Actr2* and *Actr3* were upregulated on StiffA samples (Fig. 4a), suggesting that aged CFs favour facilitating ECM remodelling through actin-mediated force exertion[32]. Although YAP translocation has classically been shown to depend on substrate stiffness, we found that ECM ligand cues contribute to the process as well, with young ECM preventing nuclear translocation in both young and aged CFs regardless of stiffness (Fig. 4c,i and Extended Data Fig. 8i,j). Our proteomics data found a lower collagen I/III ratio in young ECM (Extended Data Fig. 1q), which has been shown to promote the degradation of translocated YAP[3,10,39]. On aged ECM, young CFs enhanced YAP translocation on stiff substrates unlike aged CFs, which exhibit mechanosensing dysregulation. Furthermore, the activation of transient receptor potential vanilloid 4 (*Trpv4*), which regulates the integration of multiple extracellular cues during fibroblast activation and myofibroblast differentiation, was upregulated in aged CFs on StiffA samples (Fig. 4a), suggesting their profibrotic potential[10,29].

ECM ligand presentation outweighs stiffness in CF activation

The activation of CFs towards a myofibroblast phenotype was assessed after seeding young CFs and aged CFs on DECIPHER samples using ICC for F-actin and α-smooth muscle actin (α-SMA). Cell and nuclear morphological metrics were quantified, and CFs generally exhibited an increase in cell area and filopodia on stiffer substrates (Extended Data Fig. 9a–j), whereas ECM age did not affect the morphology. Furthermore, we observed an enhanced expression of α-SMA and stress fibre formation as a function of stiffness regardless of ECM or cell age, although to differing levels (Fig. 4j,k and Extended Data Fig. 8a–d), corresponding to previous reports that stiffness alone can activate CFs[6,8,40]. Importantly, when comparing ECM age, α-SMA was significantly reduced when CFs were plated on young ECM versus aged ECM, indicating that the composition and architecture of young ECM can prevent CF activation, overriding the stiffness cue. This is particularly evident when young CFs are cultured on StiffY samples, as well as when aged CFs are cultured on SoftY samples. Although young ECM alone cannot prevent the partial upregulation of α-SMA in aged CFs (~40% stress fibre formation on StiffY versus ~29% on SoftY), there is a clear reduction compared with aged ECM samples, highlighting the distinct mechanosensitive differences between young and aged cells. Aged ECM, on the other hand, enhanced α-SMA regardless of stiffness, with StiffA samples resulting in >64% stress fibre formation (Fig. 4j,k).

RNA-seq uncovered multiple genes that regulate CF activation in young and aged CFs as a function of ECM properties (Fig. 4l). Corresponding to the ICC data, both young and aged CFs upregulated *Acta2* (encodes α-SMA) when on aged ECM and/or high stiffness except in the case of aged CFs on StiffY (Fig. 4m; Extended Data Fig. 6a,b compares RNA-seq and RT-qPCR data). Similar correlations were observed for *Ccn2* (encodes cellular communication network factor 2), which is another known CF activation marker (Fig. 4n). *Myl9* (encodes myosin light chain 9), a downstream myofibroblast maturation marker, was upregulated in aged CFs on both SoftA and StiffA, pointing to the crucial role of ECM ligands in persistent CF activation independent of stiffness (Extended Data Fig. 3a). Taken together, we find that ECM ligand presentation can dictate myofibroblast activation state, outweighing the matrix stiffness cue.

Native ECM architecture is crucial for cellular function

ECM architecture alone has been shown to play distinct roles in driving fibroblast fate and function[7,41]. To understand the impact of native ECM architecture on fibroblast adhesion and activation, we compared DECIPHER and reconstituted young and aged dECM film substrates (Extended Data Fig. 10a). Reconstituted dECM films are conventionally utilized in ECM-related studies, but we show the complete loss of native ECM architecture due to the milling and solubilization steps (Extended Data Fig. 10b). CFs seeded on the reconstituted dECM-coated coverslips had higher α-SMA expression, stress fibre formation and focal adhesion assembly than cells on DECIPHER samples, which can be ascribed to the loss of native ECM architecture and mechanics (Extended Data Fig. 10c–i). Furthermore, young dECM alone was not sufficient to reduce or prevent the fibroblast activation of aged CFs, indicating that native architecture plays a crucial role (Extended Data Fig. 10g,i). These results underscore the importance of maintaining native ECM architecture in biomaterial approaches[42,43].

Cell and matrix age determine ECM regulation

In the healthy heart, CFs maintain matrix homeostasis by balancing protein degradation, synthesis and modification[29]. In ageing, intra- and extracellular perturbations cause dysregulation of the ECM, leading CFs to aberrantly remodel the matrix (Figs. 2c,d and 3d,e). For example, in native cardiac tissues, lysyl oxidase (LOX), which is responsible for crosslinking ECM proteins, increases with age (Extended Data Fig. 1k), with ~23% co-localized with ECM in aged tissues versus ~8% in young (Extended Data Fig. 1l). DECIPHER is capable of maintaining this age-related difference in matrix-immobilized molecules (Fig. 5b and Extended Data Fig. 1k), whereas intracellular molecules (for example, NF-κB) are completely removed due to cell removal (Extended Data Fig. 1i,j). We further confirmed the presence of accessible ligands on collagen I fibres with DECIPHER using immunogold labelling followed by SEM imaging (Fig. 5d), indicating that cells are capable of attaching to and remodelling the ECM in the scaffolds[44].

We sorted our RNA-seq data for the ECM-regulating genes. Aged CFs on StiffA scaffolds showed an upregulation of genes encoding matrix modifiers including LOX family enzymes and a downregulation of genes encoding matrix degraders including matrix metalloproteases, opposite from what is observed for young CFs on SoftY scaffolds (Fig. 5a). Enhanced LOX was also observed in aged CFs on SoftA scaffolds on both transcriptome and proteome levels (Fig. 5a,c,g,h),

https://doi.org/10.1038/s41563-025-02234-6

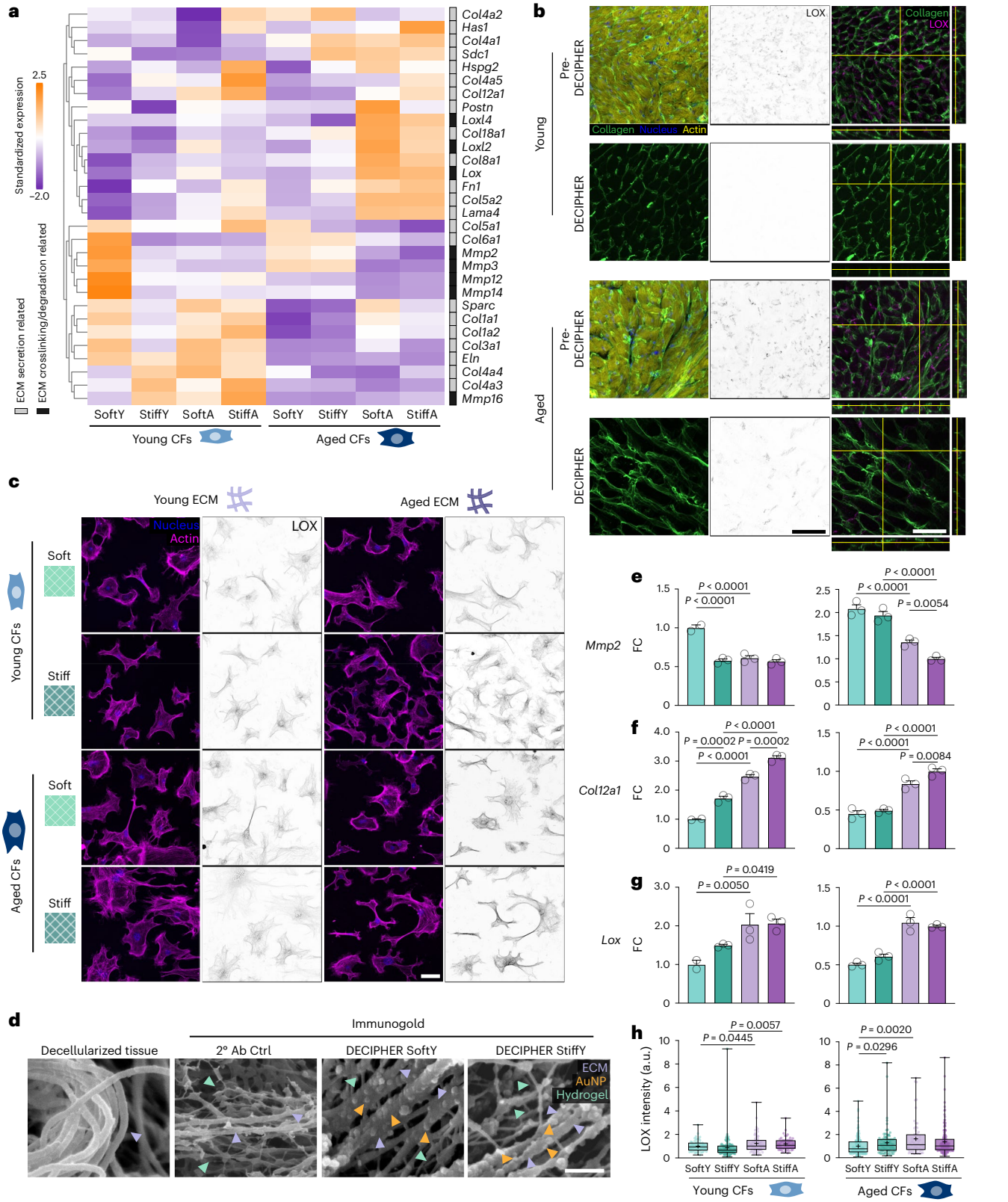

Fig. 5 | Age-related ligand and mechanical cues determine matrix regulation and remodelling. a, RNA-seq data of genes for ECM degradation, crosslinking and secretion of young and aged CFs on DECIPHER samples, with ECM protein secretion-related genes and matrix crosslinking or degradation-related genes. The colour bar indicates the row-standardized expression. **b**, DECIPHER preserves matrix-immobilized LOX in aged ECM as shown in the immunostained images (collagen, nucleus, F-actin and LOX) ($N = 3$ biological replicates for each condition). **c**, ICC of young or aged CFs on DECIPHER samples stained for nucleus, F-actin and LOX ($N = 3$ samples for each condition). **d**, DECIPHER maintains functional ligands as shown by immunogold SEM. AuNP, gold nanoparticle. 2° Ab control, immunogold 2° antibody with no primary antibody. **e**–**h**, Normalized gene expression for *Lox*, *Mmp2* and *Col12a1* given as mean ± s.e.m. One-way ANOVA with Fisher's preplanned multiple comparisons (each pair with one variable, ECM or stiffness) was used for **e**–**h**. **h**, Quantified LOX from **c** ($N = 3$ samples for each condition). Scale bars, 50 µm (**b** and **c**); 200 nm (**d**).

suggesting that both cell and matrix age increase the profibrotic potential of CFs. These results agree with our data on CF activation (Fig. 4j,k), where young ECM can override the stiffness cue in aged CFs. Profibrotic CFs increase the crosslinking of ECM, which not only directly alters the cellular behaviour through architecture-mediated mechanisms[7,45] but also exacerbates myocardial stiffening[3]. In addition, these samples showed significantly downregulated *Mmp2* and *Mmp3*, which are responsible for normal tissue ECM turnover and degradation, respectively[46] (Fig. 5e and Extended Data Fig. 3h).

In addition to ECM remodelling, the gene expression of multiple fibrillar and fibril-associated ECM proteins (for example, *Col1a1*, *Col5a1*, *Col12a1* and *Fn1*) and non-fibrillar proteins (for example, *Col8a1* and *Lama4*) were significantly upregulated in aged CFs on SoftA and StiffA samples (Fig. 5a,f and Extended Data Fig. 3i–k; Extended Data Fig. 6c–f shows a comparison of RNA-seq and RT-qPCR data), which corresponds to our mass spectrometry data (Fig. 3e and Extended Data Fig. 1o). The glycoprotein secreted protein acidic and rich in cysteine (*Sparc*), which is essential for ECM fibril formation and age-related tissue stiffening[3], was also significantly upregulated in aged CFs on SoftA and StiffA (Extended Data Fig. 3l).

Interestingly, the synthesis of ECM proteins did not display a universal increase in response to aged ECM and high stiffness. Specifically, stiffness reduced collagen III expression, which could contribute to a positive feedback loop through an increasing collagen I/III ratio. Indeed, our proteomics data identified an ~9.4% increase in collagen I/III with age, leading to the altered tissue mechanics found in other aged tissue models (Extended Data Fig. 1q,o)[3,40]. Genes encoding ECM components associated with maintaining healthy mechanics and regulating fibrotic tissue size such as elastin (*Eln*)[47] and collagen V (*Col5a1*)[5] were also downregulated (Fig. 5a), which could explain the reduction in both proteins identified in the aged cardiac ECM (Extended Data Fig. 1o). These results indicate specific combinations of matrix mechanics and the ECM age could affect the extent of matrix regulation, yet the CF age and ECM age play dominant roles.

ECM and mechanics dictate CF senescence and rejuvenation

In the ageing heart, senescence is an inevitable cellular phenotype that directly impacts organ physiology, leading to and/or accelerating cardiovascular diseases[28]. Due to the irreplaceable role of CFs in cardiac ECM deposition and remodelling, their acquisition of senescence is believed to cause an ECM imbalance, especially during the wound healing process post-acute myocardial infarction[28]. By comparing DEGs from DECIPHER groups seeded with young or aged CFs, we showed a shift of expression indicating in vitro 'cardiac ageing' of young CFs from SoftY to StiffA, as well as 'cardiac rejuvenation' of aged CFs from StiffA to SoftY (Fig. 6a,b). For young CFs, as the stiffness increases (SoftY to StiffY) or ECM ages (SoftY to SoftA), gene expression shifted towards a senescent-like phenotype that is seen on the StiffA substrate mimicking the aged heart (Fig. 6a; the unaveraged heat maps are shown in Extended Data Fig. 4b). For aged CFs, young ECM and reduced stiffness induced rejuvenation-like behaviour, with ECM playing a greater role than stiffness, as we observed for myofibroblast activation (Fig. 6b; unaveraged heat maps are shown in Extended Data Fig. 4c).

In our global KEGG analysis (Extended Data Fig. 5), DECIPHER revealed the roles of ligands and substrate stiffness in activating the cellular senescence pathways, especially for the p53 signalling pathway that has been identified as one of the most well-characterized pathways in CF senescence[28,48]. Many key senescence-associated pathways were activated concurrently with p53/p21 (encoded by *Trp53*/*Cdkn1a*), including p16 (encoded by *Cdkn2a*) and p38 mitogen-activated protein kinase, although CFs on StiffA DECIPHER samples do not demonstrate a terminally senescent phenotype in terms of collagen expression (reduced) and proinflammatory cytokines expression (enhanced) probably due to the short culture time[28,49] (Fig. 6d,f,g). On the protein level, the activation of the p53/p21 pathway was also observed, where an increased population of p53-positive cells was found on aged and stiff ECMs (Fig. 6l–n and Extended Data Fig. 8e–h). Downstream gene expression encoding senescence-associated secretory phenotype proteins that have been shown in senescent fibroblasts[28,50], including tissue inhibitor of metalloproteinase 3 (TIMP3), *Ccn1* and interleukin 6, were also enhanced (Fig. 6h–k and Extended Data Figs. 3m, 6o,p and 8k,l). Overall, these results suggest the critical roles of aged ECM and myocardial stiffness in CF activation, senescence and 'rejuvenation', with the ECM age outweighing mechanics in aged cells (Fig. 6c).

DECIPHER also uncovered the importance of cell age in the perception of ECM cues. Although we focus on specific players throughout the manuscript, we sought to understand the global regulation of age-specific cellular function by extracellular cues and, thus, analysed all DEGs identified in our RNA-seq data as a function of stiffness (comparisons: StiffY versus SoftY and StiffA versus SoftA) or ECM (comparisons: SoftA versus SoftY and StiffA versus StiffY). We found that young CFs integrate both stiffness and ECM cues to a similar extent, whereas aged CFs are less mechanosensitive but more influenced by ECM (Fig. 6e and Supplementary Note 1). In aged CFs, genes related to cardiac ageing/disease and ECM remodelling (for example, *Ccn3*, *Sned1*, *Col27a1*, *Fgfr2* and *Timp3*) were found to be regulated by ECM versus stiffness, whereas *Cmpk2* is mechanosensitive. In young CFs, multiple genes were found to be driven by both stiffness and ECM ligands (for example, *Apol9a*, *Adamts15*, *Pygo1* and *Saa3*). These findings reveal compelling prospects for rejuvenation therapies as well as underscoring the importance of matrix mechanism-targeted approaches.

Outlook

Important studies have recently uncovered the essential roles of ECM composition, architecture and mechanics in driving cellular function[2,6,45,51]. To describe the impact of ECM-specific properties, new tunable dECM-based biomaterial systems have been designed for a variety of applications including two- and three-dimensional in vitro bulk hydrogel systems, injectable in vivo hydrogel formulations and complex bioprinted scaffolds[2,52–54]. Although dECM-based biomaterials can provide faithful recapitulation of native ECM composition to some degree, preserving mechanical and architectural aspects of the native tissue remain a challenge. This is crucial because the ECM architecture has been shown to regulate cellular phenotypes and organ physiology in recent studies[7,43,45,51,55], whereas ECM mechanics have become increasingly appreciated in the field of cell biology over the past two decades[56–58].

While some dECM-based biomaterial systems can provide tunable mechanics, although within a limited range and typically much lower than the original tissue stiffness and viscoelasticity[21], the tunability depends on other ECM properties. For instance, when modifying the mechanics of lyophilized dECM, the ECM structure and composition will be influenced. On the other hand, emerging strategies in engineered heart tissues and three-dimensional dECM hydrogel models are capable of reproducing some aspects of tissue dimensionality and complexity[59], yet face challenges in throughput and reproducibility[43]. Thus, our new DECIPHER approach not only faithfully mimics the native ECM composition and architecture but also provides independent mechanical tunability spanning a greater range of physiologically relevant stiffnesses due to the fact that the hydrogel component can be synthesized from ~1 kPa to 100 kPa (refs. 17,57). Furthermore, the interpenetrating network structure of the hydrogel–ECM hybrid enhances the viscoelastic properties of the scaffolds to more accurately mimic native tissues, which improves on conventional elastic materials or reconstituted dECM materials[21].

Here we show that we can decouple the contributions of age-specific ECM ligand presentation and age-specific stiffness on cell behaviour using DECIPHER (Fig. 1). Importantly, we find that signals from the ECM can override stiffness-dependent mechanosignalling in

https://doi.org/10.1038/s41563-025-02234-6

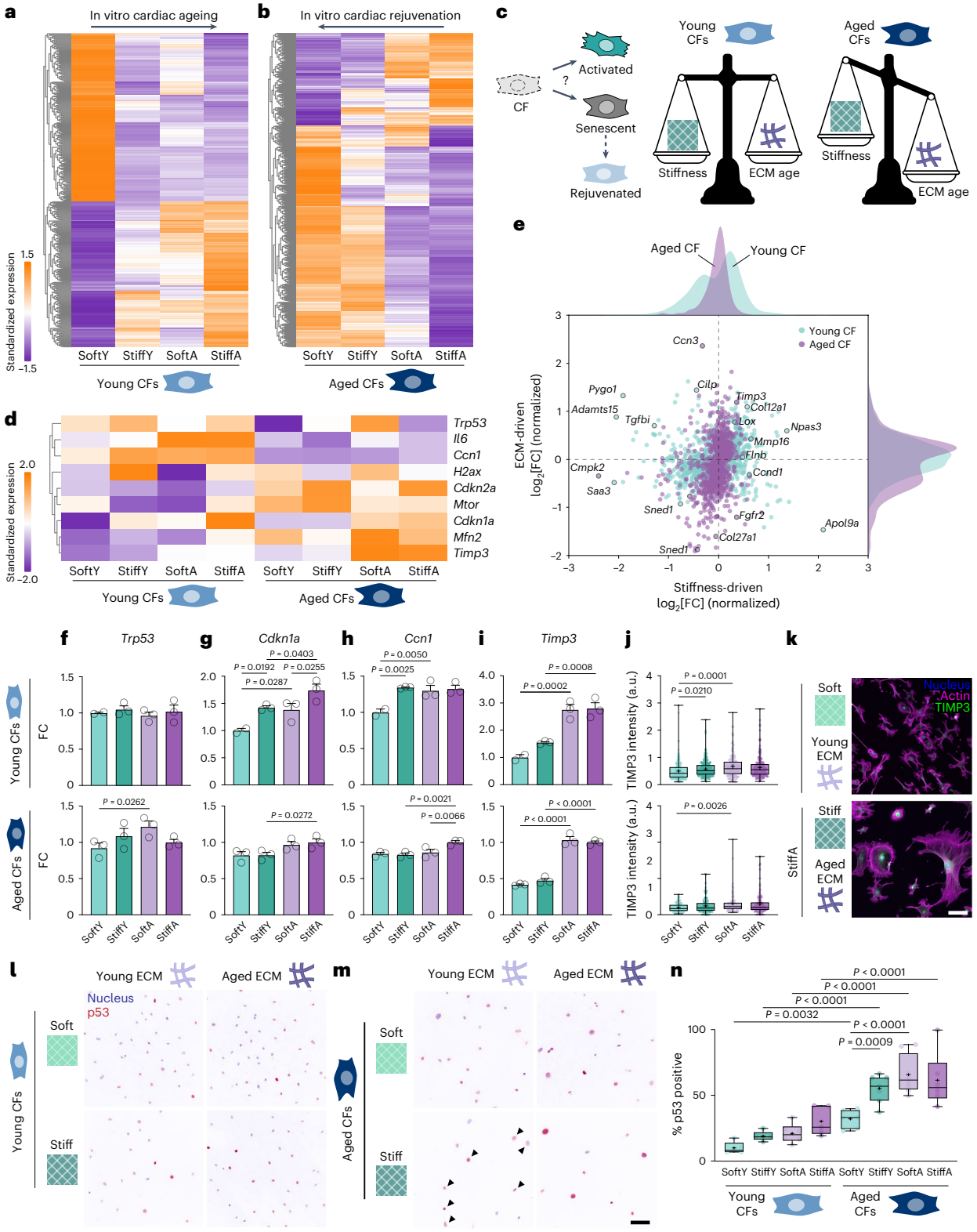

Fig. 6 | Cooperative matrix cues drive CF senescence and rejuvenation. **a**,**b**, Heat maps of RNA-seq-identified DEGs of young CFs (**a**) and aged CFs (**b**) on StiffA versus SoftY substrates. **c**, Schematic of the ECM property regulating young and aged CF functions as elucidated via DECIPHER scaffolds. **d**, Heat map of specific CF senescence regulators. For the DEGs in **a** and **b**, FC > 1.5 and $P < 0.05$. **e**, Normalized $\log_2$[FC] values of all DEGs (957) identified in the DECIPHER samples driven by stiffness or ECM for young and aged CFs. Probability density of stiffness- and ECM-driven genes is shown on the respective axis for young and aged CFs. **f**–**i**, Normalized gene expression for *Trp53* (**f**), *Cdkn1a* (**g**), *Ccn1* (**h**) and *Timp3* (**i**) are mean ± s.e.m. **j**–**n**, ICC of CFs on DECIPHER samples for nucleus, F-actin and TIMP3 (**j** and **k**) or p53 (**l** and **m**) and quantified in **n**. The arrows in **l** indicate the example nuclei that are above the p53+ intensity threshold. $N = 3$ samples for each condition (**j** and **n**). In **a**, **b** and **d**, the colour bar indicates the row-standardized expression. One-way ANOVA with Fisher's preplanned multiple comparisons (each pair with one variable, ECM or stiffness) was used in **f**–**j** and **n**. Scale bar, 100 µm (**k**–**m**).

age-related CF activation, matrix remodelling and the acquisition of senescent-like phenotypes (Fig. 6c), finding key roles of ligand-specific cues that have been shown to dictate other cellular behaviours, including collective migration and stem cell fate[60,61]. We further show that young ECM contributes to the rejuvenation potential of aged CFs through distinct signalling pathways, overriding substrate mechanics (Fig. 6e).

The ultimate application of this DECIPHER platform is to identify new targets for matrix-based rejuvenation strategies, and we found that young, soft ECM could enhance the rejuvenation potential of aged CFs. How CFs integrate biochemical, architectural and mechanobiological signalling cues to determine their phenotypical transition towards an aged, dysfunction state still requires further investigation with this system, and future studies will focus on the dynamics of this process, as previous reports have highlighted the importance of time dependence in cardiac function[62,63]. Taken together, we describe here a novel material platform that has widespread applicability to other tissues and/or disease types for which cell–ECM interactions play a crucial role.

Online content

Any methods, additional references, Nature Portfolio reporting summaries, source data, extended data, supplementary information, acknowledgements, peer review information; details of author contributions and competing interests; and statements of data and code availability are available at https://doi.org/10.1038/s41563-025-02234-6.

References

1. Nance, M. E. et al. Attenuated sarcomere lengthening of the aged murine left ventricle observed using two-photon fluorescence microscopy. *Am. J. Physiol. Circ. Physiol.* **309**, H918–H925 (2015).
2. Ozcebe, S. G., Bahcecioglu, G., Yue, X. S. & Zorlutuna, P. Effect of cellular and ECM aging on human iPSC-derived cardiomyocyte performance, maturity and senescence. *Biomaterials* **268**, 120554 (2021).
3. Meschiari, C. A., Ero, O. K., Pan, H., Finkel, T. & Lindsey, M. L. The impact of aging on cardiac extracellular matrix. *Geroscience* **39**, 7–18 (2017).
4. Antia, M., Baneyx, G., Kubow, K. E. & Vogel, V. Fibronectin in aging extracellular matrix fibrils is progressively unfolded by cells and elicits an enhanced rigidity response. *Faraday Discuss.* **139**, 229–249 (2008).
5. Yokota, T. et al. Type V collagen in scar tissue regulates the size of scar after heart injury. *Cell* **182**, 545–562 (2020).
6. Herum, K. M., Choppe, J., Kumar, A., Engler, A. J. & McCulloch, A. D. Mechanical regulation of cardiac fibroblast profibrotic phenotypes. *Mol. Biol. Cell* **28**, 1871–1882 (2017).
7. Wang, Z. et al. Snake venom-defined fibrin architecture dictates fibroblast survival and differentiation. *Nat. Commun.* **14**, 1029 (2023).
8. Tomasek, J. J., Gabbiani, G., Hinz, B., Chaponnier, C. & Brown, R. A. Myofibroblasts and mechano-regulation of connective tissue remodelling. *Nat. Rev. Mol. Cell Bio.* **3**, 349–363 (2002).
9. Talman, V. & Ruskoaho, H. Cardiac fibrosis in myocardial infarction—from repair and remodeling to regeneration. *Cell Tissue Res.* **365**, 563–581 (2016).
10. Angelini, A., Trial, J., Ortiz-Urbina, J. & Cieslik, K. A. Mechanosensing dysregulation in the fibroblast: a hallmark of the aging heart. *Ageing Res. Rev.* **63**, 101150 (2020).
11. Weber, K. T., Sun, Y., Bhattacharya, S. K., Ahokas, R. A. & Gerling, I. C. Myofibroblast-mediated mechanisms of pathological remodelling of the heart. *Nat. Rev. Cardiol.* **10**, 15–26 (2013).
12. Cieslik, K. A., Trial, J., Carlson, S., Taffet, G. E. & Entman, M. L. Aberrant differentiation of fibroblast progenitors contributes to fibrosis in the aged murine heart: role of elevated circulating insulin levels. *Faseb J.* **27**, 1761–1771 (2013).
13. Chen, Z. et al. Intrafibrillar crosslinking enables decoupling of mechanical properties and structure of a composite fibrous hydrogel. *Adv. Mater.* **36**, e2305964 (2023).
14. Cunha, C. Bda et al. Influence of the stiffness of three-dimensional alginate/collagen-I interpenetrating networks on fibroblast biology. *Biomaterials* **35**, 8927–8936 (2014).
15. Berger, A. J., Linsmeier, K. M., Kreeger, P. K. & Masters, K. S. Decoupling the effects of stiffness and fiber density on cellular behaviors via an interpenetrating network of gelatin-methacrylate and collagen. *Biomaterials* **141**, 125–135 (2017).
16. Chung, K. et al. Structural and molecular interrogation of intact biological systems. *Nature* **497**, 332–337 (2013).
17. Tse, J. R. & Engler, A. J. Preparation of hydrogel substrates with tunable mechanical properties. *Curr. Protoc. Cell Biol.* **47**, 10.16.1–10.16.16 (2010).
18. Crapo, P. M., Gilbert, T. W. & Badylak, S. F. An overview of tissue and whole organ decellularization processes. *Biomaterials* **32**, 3233–3243 (2011).
19. Großkopf, H. et al. Identification of intracellular glycosaminoglycan-interacting proteins by affinity purification mass spectrometry. *Biol. Chem.* **402**, 1427–1440 (2021).
20. Wershof, E. et al. A FIJI macro for quantifying pattern in extracellular matrix. *Life Sci. Alliance* **4**, e202000880 (2021).
21. Chaudhuri, O., Cooper-White, J., Janmey, P. A., Mooney, D. J. & Shenoy, V. B. Effects of extracellular matrix viscoelasticity on cellular behaviour. *Nature* **584**, 535–546 (2020).
22. Ma, Y. et al. Viscoelastic cell microenvironment: hydrogel-based strategy for recapitulating dynamic ECM mechanics. *Adv. Funct. Mater.* **31**, 2100848 (2021).
23. Bovio, S., Long, Y. & Monéger, F. Use of atomic force microscopy to measure mechanical properties and turgor pressure of plant cells and plant tissues. *J. Vis. Exp.* https://doi.org/10.3791/59674 (2019).
24. Nakayama, K. H., Batchelder, C. A., Lee, C. I. & Tarantal, A. F. Decellularized rhesus monkey kidney as a three-dimensional scaffold for renal tissue engineering. *Tissue Eng. A* **16**, 2207–2216 (2010).
25. Fathi, I. et al. Decellularized whole-organ pre-vascularization: a novel approach for organogenesis. *Front. Bioeng. Biotechnol.* **9**, 756755 (2021).
26. Sun, A. R., Hengst, R. M. & Young, J. L. All the small things: nanoscale matrix alterations in aging tissues. *Curr. Opin. Cell Biol.* **87**, 102322 (2024).
27. Jeong, D. et al. Matricellular protein CCN5 reverses established cardiac fibrosis. *J. Am. Coll. Cardiol.* **67**, 1556–1568 (2016).
28. Chen, M. S., Lee, R. T. & Garbern, J. C. Senescence mechanisms and targets in the heart. *Cardiovasc. Res.* **118**, 1173–1187 (2021).
29. Pesce, M. et al. Cardiac fibroblasts and mechanosensation in heart development, health and disease. *Nat. Rev. Cardiol.* **20**, 309–324 (2022).
30. Sun, S.-N. et al. G-MDSCs promote aging-related cardiac fibrosis by activating myofibroblasts and preventing senescence. *Cell Death Dis.* **12**, 594 (2021).
31. Zhang, Y. et al. Cellinker: a platform of ligand–receptor interactions for intercellular communication analysis. *Bioinformatics* **37**, 2025–2032 (2021).
32. Kanchanawong, P. & Calderwood, D. A. Organization, dynamics and mechanoregulation of integrin-mediated cell–ECM adhesions. *Nat. Rev. Mol. Cell Biol.* **24**, 142–161 (2022).
33. He, J., Fang, B., Shan, S. & Li, Q. Mechanical stiffness promotes skin fibrosis through piezo1-mediated arginine and proline metabolism. *Cell Death Discov.* **9**, 354 (2023).

34. Rao, L.-Z. et al. IL-24 deficiency protects mice against bleomycin-induced pulmonary fibrosis by repressing IL-4-induced M2 program in macrophages. *Cell Death Differ.* **28**, 1270–1283 (2021).
35. Goldsmith, E. C., Bradshaw, A. D., Zile, M. R. & Spinale, F. G. Myocardial fibroblast–matrix interactions and potential therapeutic targets. *J. Mol. Cell. Cardiol.* **70**, 92–99 (2014).
36. Li, R. & Frangogiannis, N. G. Integrins in cardiac fibrosis. *J. Mol. Cell. Cardiol.* **172**, 1–13 (2022).
37. Roca-Cusachs, P., Gauthier, N. C., Rio, Adel & Sheetz, M. P. Clustering of α5β1 integrins determines adhesion strength whereas αvβ3 and talin enable mechanotransduction. *Proc. Natl Acad. Sci. USA* **106**, 16245–16250 (2009).
38. Schiller, H. B. et al. β1- and αv-class integrins cooperate to regulate myosin II during rigidity sensing of fibronectin-based microenvironments. *Nat. Cell Biol.* **15**, 625–636 (2013).
39. Stanton, A. E., Tong, X. & Yang, F. Extracellular matrix type modulates mechanotransduction of stem cells. *Acta Biomater.* **96**, 310–320 (2019).
40. Ma, Y., Iyer, R. P., Jung, M., Czubryt, M. P. & Lindsey, M. L. Cardiac fibroblast activation post-myocardial infarction: current knowledge gaps. *Trends Pharm. Sci.* **38**, 448–458 (2017).
41. Bugg, D. et al. Infarct collagen topography regulates fibroblast fate via p38-yes-associated protein transcriptional enhanced associate domain signals. *Circ. Res.* **127**, 1306–1322 (2020).
42. Ozcebe, S. G. & Zorlutuna, P. In need of age-appropriate cardiac models: impact of cell age on extracellular matrix therapy outcomes. *Aging Cell* **22**, e13966 (2023).
43. Cho, S., Discher, D. E., Leong, K. W., Vunjak-Novakovic, G. & Wu, J. C. Challenges and opportunities for the next generation of cardiovascular tissue engineering. *Nat. Methods* **19**, 1064–1071 (2022).
44. Klein, J. et al. Proteasix: a tool for automated and large-scale prediction of proteases involved in naturally occurring peptide generation. *Proteomics* **13**, 1077–1082 (2013).
45. Devarasou, S., Kang, M., Kwon, T. Y., Cho, Y. & Shin, J. H. Fibrous matrix architecture-dependent activation of fibroblasts with a cancer-associated fibroblast-like phenotype. *ACS Biomater. Sci. Eng.* **9**, 280–291 (2023).
46. DeLeon-Pennell, K. Y., Meschiari, C. A., Jung, M. & Lindsey, M. L. Chapter two—matrix metalloproteinases in myocardial infarction and heart failure. *Prog. Mol. Biol. Transl. Sci.* **147**, 75–100 (2017).
47. Mizuno, T., Yau, T. M., Weisel, R. D., Kiani, C. G. & Li, R.-K. Elastin stabilizes an infarct and preserves ventricular function. *Circulation* **112**, I81–I88 (2005).
48. Meyer, K., Hodwin, B., Ramanujam, D., Engelhardt, S. & Sarikas, A. Essential role for premature senescence of myofibroblasts in myocardial fibrosis. *J. Am. Coll. Cardiol.* **67**, 2018–2028 (2016).
49. Zhu, F. et al. Senescent cardiac fibroblast is critical for cardiac fibrosis after myocardial infarction. *PLoS ONE* **8**, e74535 (2013).
50. Coppé, J.-P., Desprez, P.-Y., Krtolica, A. & Campisi, J. The senescence-associated secretory phenotype: the dark side of tumor suppression. *Annu. Rev. Pathol.* **5**, 99–118 (2010).
51. DePalma, S. J. et al. Matrix architecture and mechanics regulate myofibril organization, costamere assembly, and contractility in engineered myocardial microtissues. *Adv. Sci.* **11**, 2309740 (2024).
52. Basara, G., Ozcebe, S. G., Ellis, B. W. & Zorlutuna, P. Tunable human myocardium derived decellularized extracellular matrix for 3D bioprinting and cardiac tissue engineering. *Gels* **7**, 70 (2021).
53. Kim, H. et al. Light-activated decellularized extracellular matrix-based bioinks for volumetric tissue analogs at the centimeter scale. *Adv. Funct. Mater.* **31**, 2011252 (2021).
54. Spang, M. T. et al. Intravascularly infused extracellular matrix as a biomaterial for targeting and treating inflamed tissues. *Nat. Biomed. Eng.* **7**, 94–109 (2023).
55. Umehara, T. et al. Female reproductive life span is extended by targeted removal of fibrotic collagen from the mouse ovary. *Sci. Adv.* **8**, eabn4564 (2022).
56. Engler, A. J., Sen, S., Sweeney, H. L. & Discher, D. E. Matrix elasticity directs stem cell lineage specification. *Cell* **126**, 677–689 (2006).
57. Hadden, W. J. et al. Stem cell migration and mechanotransduction on linear stiffness gradient hydrogels. *Proc. Natl Acad. Sci. USA* **114**, 5647–5652 (2017).
58. Iskratsch, T., Wolfenson, H. & Sheetz, M. P. Appreciating force and shape—the rise of mechanotransduction in cell biology. *Nat. Rev. Mol. Cell Biol.* **15**, 825–833 (2014).
59. Min, S. et al. Versatile human cardiac tissues engineered with perfusable heart extracellular microenvironment for biomedical applications. *Nat. Commun.* **15**, 2564 (2024).
60. Russo, J. D. et al. Integrin α5β1 nano-presentation regulates collective keratinocyte migration independent of substrate rigidity. *eLife* **10**, e69861 (2021).
61. Trappmann, B. et al. Extracellular-matrix tethering regulates stem-cell fate. *Nat. Mater.* **11**, 642–649 (2012).
62. Young, J. L. & Engler, A. J. Hydrogels with time-dependent material properties enhance cardiomyocyte differentiation in vitro. *Biomaterials* **32**, 1002–1009 (2011).
63. Walker, C. J. et al. Nuclear mechanosensing drives chromatin remodelling in persistently activated fibroblasts. *Nat. Biomed. Eng.* **5**, 1485–1499 (2021).

[1]Mechanobiology Institute (MBI), National University of Singapore, Singapore, Singapore. [2]Department of Biomedical Engineering, College of Design and Engineering, National University of Singapore, Singapore, Singapore. [3]Department of Biological Sciences, National University of Singapore, Singapore, Singapore. [4]Cardiovascular-Metabolic Disease Translational Research Programme, Yong Loo Lin School of Medicine, National University of Singapore, Singapore, Singapore. [5]Cardiovascular Research Institute, National University Healthcare Systems, Singapore, Singapore. ✉e-mail: biejly@nus.edu.sg

Methods

Preparation of coverslips and hydrogel solutions

Coverslips (ϕ = 15 mm) were cleaned via sonication during progressive washes with acetone, ethanol and MilliQ water for 10 min each and then air dried. For hydrogel attachment, coverslips were treated with a UV/ozone cleaner (Bioforce ProCleaner Plus) for 5 min followed by immersion in a solution containing 20 ml of ethanol, 600 µl of 10% acetic acid and 200 µl of 3-trimethoxysilylpropylmethacrylate for 5 min. Coverslips were then washed twice in ethanol and air dried before placing onto the tissue slice and hydrogel solution. The PA-based hydrogels used in this study mimicking the young (~10 kPa) and aged (~40 kPa) cardiac tissue stiffness were labelled as 'soft' and 'stiff' for easy reference, with their composition detailed in Supplementary Table 1. Prepared solutions of acrylamide and bis-acrylamide were prereacted with formaldehyde at 4 °C for 3 h at a stoichiometric ratio of >10:1 to ensure no excess formaldehyde in the solution[16]. Before hydrogel formation, Irgacure 2959 (2-hydroxy-4′-(2-hydroxyethoxy)-2-methylpropiophenone, Sigma-Aldrich) was added for UV photoinitiation. For hydrogel visualization experiments, separate samples of 10-kPa solution were made with Nile Blue-tagged acrylamide (Polysciences no. 25395-100) at 1:1,000.

Tissue handling, slicing and stabilization

Young (1–2 months) and aged (18–24 months) hearts were extracted from C57BL/6J strain female mice (obtained via NUS Animal Tissue Sharing Programme under Institutional Animal Care and Use Committee, National University of Singapore) after euthanasia and quickly transferred to sterile 1× phosphate-buffered saline (PBS) to minimize blood clot formation. The major vascular tissues superiorly attached to the hearts were then carefully removed with sterile surgical instruments. Before slicing the heart using a vibratome (Leica VT 1200S), the heart was embedded in a 4% low-melting-point agarose (Invitrogen) solution in sterile 1× PBS, with the orientation adjusted such that coronal slices are obtained during slicing. Agarose was kept on ice until solidified, attached to the slicing stage with superglue and loaded onto the vibratome. Following the initial trimmings of the agarose cube, the slicing speed was set to 0.18 mm s^{-1} and 150-µm slice thickness.

After tissue sectioning, vibratome slices were carefully transferred to a hydrophobic glass slide (dichlorodimethylsilane-treated) in a humid condensation chamber. The agarose surrounding the cardiac tissue was gently removed, as well as any excess liquid on the cardiac slices, by wicking away at the edges with a Kimwipe. Then, 21 ± 2 µl of the hydrogel solutions were added to each 150-µm-thick cardiac slice (solution volume was adjusted based on the volume of the tissue to fill the coverslip area) and incubated at 4 °C for 60 min in the dark. Crosslinking was then initiated using the same parameters as the plain hydrogel samples (35 mW cm^{-2} for 3 min). The samples were then transferred to a 12-well plate and kept in sterile MilliQ water at 4 °C before decellularization.

Decellularization of PA-stabilized cardiac tissue sections

All solutions were aseptically prepared, and all the experiment areas were sterilized frequently with 70% ethanol to prevent microbial contamination. SDC (Sigma-Aldrich) was dissolved in MilliQ water at 5% (w/v). The PA-stabilized tissue samples were exchanged with 2 ml per well of SDC solution and kept on a gentle shaker at room temperature for 2.5 days with one exchange at 24 h. The samples were then washed with MilliQ water and 10,000 U penicillin/streptomycin (pen/strep, Gibco) for 2 h. Subsequently, 2 ml of 300 kU ml^{-1} DNase-I solution (Sigma-Aldrich; dissolved in 0.15-M NaCl supplemented with 5-mM $CaCl_2$ and 1% pen/strep) was added to each sample after discarding the pen/strep and gently shaking for 3.5 days followed by a final MilliQ water wash for 2 h.

Mass spectrometry

Freshly harvested and sliced cardiac tissues from young (2 months) or aged (24 months) mice were decellularized using the same protocol as described in the previous section using SDC and DNase-I. Then, dECM samples were snap frozen using liquid nitrogen and shipped on dry ice to BGI Genomics for further extraction steps followed by tandem-mass-tag-based quantitative mass spectrometry. Samples were ultrasonicated in an extraction cocktail containing EDTA and SDS-lysate buffer (7-M urea, 2-M thiourea, 20-mM Tris-HCl, pH 8.0) for 5 min on ice and centrifuged at 25,000*g* for 15 min at 4 °C. The supernatant was incubated in dithiothreitol (10 mM) and incubated at 37 °C for 30 min, followed by iodoacetamide (55 mM) treatment for 45 min. Proteins were precipitated using cold acetone at −20 °C and collected by a centrifuge at 25,000*g* for 15 min at 4 °C. Protein pellets were resuspended in a lysis buffer without SDS-lysate and centrifuged again to remove any insoluble residues. Quality control was performed after each round of protein extraction by Bradford quantification and sodium dodecyl sulfate-polyacrylamide gel electrophoresis. Then, 0.5-M tetraethylammonium bromide was used to collect the protein by centrifuging three rounds at 12,000*g* and 20 °C, followed by trypsin digestion. Subsequently, peptides were labelled with a tandem mass tag for 2 h at room temperature, fractionized using Shimadzu LC-20AB liquid-phase system and freeze dried. The dried peptide samples were then injected into a Thermo Scientific UltiMate 3000 UHPLC connected to a mass spectrometer (Thermo Scientific Q-Exactive HF X). The ion source voltage was set to 1.9 kV; the MS1 scanning range was 350–1,500 m/z and the resolution was set to 60,000; the starting m/z of MS2 was fixed at 100 and the resolution was 15,000.

Reconstituted solubilized dECM substrates

Young (1–2 months) or aged (18–24 months) murine hearts were sliced and decellularized using the same protocol as described in the previous section with SDC and DNase-I. The dECM samples were then snap frozen in liquid nitrogen and lyophilized overnight. Lyophilized dECM was then pulverized and solubilized[2]. Briefly, 1 mg ml^{-1} pepsin (Roche) was dissolved in 0.1-M HCl and added to milled dECM at a 10:1 ratio (w/w, dECM:pepsin) followed by constant stirring at room temperature. When a homogeneous solution was obtained, 1-M NaOH was used to neutralize the supernatant after removing insoluble residues. A Pierce BCA Protein Assay Kit (Thermo Scientific) was then used to quantify the total ECM protein amount. Solubilized dECM was diluted to 1 mg ml^{-1} with 1× PBS, coated onto 15-mm coverslips and incubated for 30 min in a condensation chamber at 37 °C.

ECM quantitative compositional assays

Quantitative compositional analyses of samples were performed for DNA, sGAG and collagen content. The sample's DNA was extracted using phenol–chloroform and kept at −20 °C until applying the PicoGreen dsDNA assay kit (Invitrogen). Total sGAGs of the samples were obtained via papain (Sigma-Aldrich) extraction followed by Blyscan sGAG assay (Biocolor). For collagen quantification, the samples were first homogenized and hydrolysed in concentrated HCl at 120 °C for 3 h before being quantified using a hydroxyproline assay kit (Sigma-Aldrich). A microplate reader (Promega GloMax) was used for all the assays. Duplicate technical replicates with N = 3 biological replicates were measured along with standard curves for quantification, according to the suppliers' instructions.

IHC

IHC of the native tissue sections and DECIPHER samples was carried out for ECM components and cellular structures (antibodies and dilutions are detailed in Supplementary Table 2). Briefly, samples were fixed with 4% formaldehyde (Sigma-Aldrich) and rinsed with 1× PBS before blocking and permeabilizing with 2% bovine serum albumin (BSA; Sigma-Aldrich) in 0.2% Triton X-100 (Sigma-Aldrich) for 30 min. The samples were then incubated with primary antibodies in 2% BSA on a gentle shaker at room temperature for 3 days followed by three times

of 1× PBS washing and incubation of secondary antibodies and CF Phalloidin (Biotium) staining for 1 h at room temperature in the dark. To label any denatured collagen, Cy3-conjugated collagen hybridizing peptide (R-CHP, 3Helix) was diluted to 5 µM and used to stain the samples after CNA35 labelling according to the product's instructions[64,65]. The samples were further stained with Hoechst 33342 (Invitrogen) and mounted using Fluoromount-G (Invitrogen). For hydrogel visualization experiments using Nile Blue-tagged acrylamide, the samples were co-stained with CNA35.

Immunogold labelling and SEM

SEM was used to visualize the nanoarchitecture of PA-hydrogel-stabilized cardiac tissue after decellularization (DECIPHER samples) and native cardiac tissue cryosections cut at 10 µm (Leica CM1950) from snap-frozen fresh young hearts embedded in OCT (Tissue-Tek, Sakura Finetek). For immunogold labelling, the samples were first fixed with 4% formaldehyde and rinsed with 1× PBS before blocking with 3% goat serum and 1% BSA for 30 min. Endogenous mouse IgG was blocked followed by incubation with a site-specific primary antibody. Samples were then rinsed with PBS + 0.1% Tween 20 and incubated with secondary antibody conjugated with 10-nm gold (Invitrogen) according to the supplier's instructions. Immunogold-labelled samples were then rinsed and enhanced using Nanoprobes GoldEnhance EM Plus kit to improve the SEM visualization. Before SEM, all the samples were fixed with glutaraldehyde (Sigma-Aldrich) followed by dehydration using a series of ethanol exchanges of increasing concentration and dried using a Critical Point Dryer (Tousimis Autosamdri-815). The samples were coated with 8-nm platinum (for native tissue samples and unstained DECIPHER samples) or carbon (for immunogold samples) before being imaged using a Hitachi Regulus 8230 FE-SEM at 1–3-kV acceleration voltage and 8-mm working distance.

Nanoindentation

To obtain the Young modulus of PA hydrogels and PA-hydrogel-stabilized cardiac tissue slices pre- and post-DECIPHER, the samples were attached to glass-bottom Petri dishes with superglue. For native tissues, vibratome slices were prepared at 500 µm and attached to dishes with GLUture (World Precision Instruments, 503763). All the samples were then indented with the Optics11 Life Chiaro Nanoindenter using a spherical probe (k = 0.5 N m^{-1}; tip radius, 50 µm). To minimize sample–probe adhesion, 1% Pluronic (Sigma-Aldrich) solution was used to coat the probe before the experiments. Calibration was carried out against a glass dish. Quasi-static matrix scans were performed with a 2-µm indentation depth and step sizes of 500 µm (native tissue, PA-stabilized tissue and DECIPHER samples) or 800 µm (plain PA hydrogel samples). The Young modulus of each data point was obtained from the Hertzian contact model with Poisson's ratio ν = 0.5 in the Optics11 DataViewer software (v.2.7.0).

Dynamic mechanical analysis was used to measure the storage and loss moduli with a 2-µm indentation depth and 300-nm oscillation amplitude. The maximum indentation depth in the dynamic mechanical analysis was reached at 0.1 s, followed by 20-s relaxation, and then an oscillatory frequency sweep at 1, 2, 4 and 10 Hz was performed. Five periods of oscillation were carried out for all frequencies, except in the 10-Hz experiment, where ten periods were used to ensure a minimum oscillation time of 1 s. The storage modulus (E') and loss modulus (E'') were calculated using the Optics11 DataViewer software.

Correlative confocal–AFM

AFM calibrations and measurements were performed after confocal imaging[23]. Briefly, a JPK NanoWizard 4 XP Bioscience AFM system with a BioMAT Workstation (Bruker) were used in conjunction with an upright Stellaris 8 laser scanning confocal microscope (Leica) equipped with a customized BioMAT shuttle stage, which enabled the precise positioning and alignment of the measured areas for the sequential confocal–AFM scans. A triangular cantilever (Nanoworld, Pyrex-Nitride Probe) with a nominal spring constant of 0.32 N m^{-1} with a pyramidal tip of 35° face half-angle were used. Calibration for deflection sensitivity and the spring constant was done under water with the contact-based calibration mode on a glass slide. The manufacturer's calibration slide (Bruker) was used to optically align the confocal and AFM scan areas using the DirectOverlay function of the JPK NanoWizard data processing software (v.8.0.144), and minor alignment corrections were performed manually in post-processing.

The DECIPHER and native tissue samples were first stained with CNA35 without fixation (to provide live visualization of the collagen ECM) and imaged under the confocal microscope to obtain a three-dimensional stack and locate the regions of interest of the exposed ECM (collagen) fibres and the surrounding hydrogel (for DECIPHER). The samples were then transferred to the AFM system on the shuttle stage to perform surface topographic scans using the cells in the liquid quantitative imaging mode (force setpoint, 15–25 µN; indentation depth, 0.5–2 µm; Z speed, 25–40 µm; Z length, 4–5 µm; scan rate, 25–40 kHz; pixel time, 20 ms; x–y resolution: ~312.50 nm per pixel). The scan sizes ranged in 25 × 25 µm^2 to 50 × 50 µm^2 with a resolution from 32 × 32 pixels to 80 × 80 pixels, respectively. After scanning, all the quantitative imaging images and force–distance curves were analysed in the JPK NanoWizard data processing software (v.8.0.144). The force–distance curves underwent baseline correction and smoothing before contact-point determination and fitting for Young's moduli. The apparent Young's modulus for each pixel in the quantitative imaging image was obtained by fitting a Sneddon contact model for the whole approach curve with ν = 0.5 to obtain the modulus maps. For quantification, three to five regions of interest with sizes of 4–6.25 µm^2 were selected on the fibre and on the surrounding gel (for DECIPHER) to derive the regional average moduli.

Primary CF isolation and in vitro culture

The use of animals was approved by the Institutional Animal Care and Use Committee (protocol no. R22-0579), National University of Singapore. Mice are housed in individually ventilated cages with sex-matched littermates, 12-h light–dark cycles, ambient temperature (20–24 °C) and humidity (30%–70%), and ad libitum food and water supply. Primary young and aged CFs were extracted[66] from female young (1–2 months) and aged (24 months) C57BL/6J murine hearts, respectively. Briefly, mouse hearts were perfused with cardiac digestion buffers by intraventricular injection. Three rounds of gravity settling were applied to separate cardiomyocyte and non-cardiomyocyte cells. Non-cardiomyocyte cells were seeded onto untreated tissue culture plastic and washed after 1 h to enrich for CFs. CFs were expanded in CF growth medium (Dulbecco's modified Eagle's medium/high glucose (Cytiva) supplemented with 15% fetal bovine serum (Gibco)), penicillin (100 U ml^{-1}), streptomycin (100 µg ml^{-1}, Nacalai Tesque), FGF2 (10 ng ml^{-1}, Stemcell Technologies) and SB-431542 (5 µM, Targetmol).

All cells used in the in vitro studies were from passages 2 or 3. Before cell seeding, all the DECIPHER samples were immersed in sterile 1× PBS overnight, UV sterilized in a biosafety cabinet for 60 min and equilibrated in full maintenance media for 30 min. The isolated cells were seeded at 10,000 cells per well of a 12-well plate in 1 ml of culture media (Dulbecco's modified Eagle's medium + 1% fetal bovine serum + 1% pen/strep) onto DECIPHER samples and kept in a 37 °C, 5% CO_2, humidified incubator for a culture period of 2 days. Cell culture supernatant was regularly tested negative for mycoplasma contamination using InvivoGen's MycoStrip.

ICC

After culturing, cells were rinsed in sterile 1× PBS three times and then fixed with 4% formaldehyde for 15 min, permeabilized with 0.1% Triton X-100 for 15 min and blocked with 2% BSA for 30 min for ICC. For mouse-anti-mouse primary antibodies, 2% goat serum with 1% BSA

was used instead as the blocking and staining buffer, with an extra step of blocking endogenous mouse IgG for 1 h at room temperature to reduce the background noise from the ECM. Samples were stained with primary antibodies (Supplementary Table 2) overnight at 4 °C in 2% BSA, rinsed three times in 1× PBS + 0.1% Tween 20, followed by secondary antibodies and CF Phalloidin for 1 h at room temperature diluted in 2% BSA. The samples were washed with PBS + 0.1% Tween 20 three times (5 min each) and stained with Hoechst 33342 in H_2O for 10 min at room temperature before three rounds of water rinses and mounted with Fluoromount-G.

Low-input bulk RNA-seq

All the reagents are DNase/RNase/protease free and diluted with HyPure Molecular Biology Grade Water (Cytiva). Cells attached to the DECIPHER samples were lysed using TRIzol (Ambion) after scraping away the excess hydrogel region and kept under −80 °C pending RNA extraction. To further provide baseline (in vivo) control groups, freshly isolated young/aged primary CFs were directly lysed with TRIzol after extraction. Total RNA of the samples was extracted using a chloroform–isopropanol approach according to the supplier's instructions. Briefly, chloroform was added to the lysed cell samples after thawing and vigorously mixed and centrifuged at 14,000*g* for 15 min before the supernatant was collected. RNA was then precipitated using cold isopropanol, collected by centrifugation at 14,000*g* for 15 min and washed twice with precooled 75% ethanol followed by centrifugation at 14,000*g* for 10 min. The RNA samples were air dried for 5–10 min before being dissolved in HyPure water and processed for quality control with TapeStation High Sensitivity RNA ScreenTape Analysis. Sample RNA with an RNA integrity number (RIN^e) larger than 8.5 (high quality) was applied to NEBNext Single Cell/Low Input RNA Library Prep Kit for Illumina for cDNA synthesis and sequence-ready library preparation according to the supplier's instructions. Specifically, 20 ng of total RNA from each sample was used for cDNA synthesis and eight PCR cycles were used for cDNA amplification. The libraries were indexed with NEBNext Multiplex Oligos for Illumina (96 Unique Dual Index Primer Pairs Set 2) and submitted to NovogeneAIT Genomics (Singapore) for sequencing on the Illumina NovaSeq 6000 system.

Multiplex RT-qPCR

RNA extraction and quality control were performed as described in the RNA-seq section. Subsequently, a Reliance One-Step Multiplex RT-qPCR Supermix (Bio-Rad) was used to perform reverse transcription and qPCR by PrimePCR Probe Assays built in a Bio-Rad CFX96 Real-Time PCR Detection System. The thermal cycling protocol was set to the Bio-Rad product sheet default: 50 °C for 10 min (RT), 95 °C for 10 min (DNA polymerase activation and template denaturation) and 40 cycles of 95 °C for 10 s followed by 60 °C for 30 s (amplification). All the PrimePCR Probes used in this study were purchased from Bio-Rad (Supplementary Table 3), which had been optimally designed and validated for the multiplex qPCR supermix and experiments.

Imaging and analysis

The IHC and ICC samples were observed using a Nikon A1R scanning laser confocal microscope (×40 and ×60 water-immersion objectives, NIS Elements v. 5.30.05) or Oxford Instruments BC43 spinning-disc confocal microscope (×20 and ×40 air objectives, Fusion v. 2.3) and subsequently imported to Fiji. A Fiji macro, TWOMBLI, was used to quantify the ECM architectural changes post-decellularization and in ageing with the default parameters[20]. Confocal images from pre- and post-decellularized samples were analysed for lacunarity, endpoints, branch points, fractal dimension, alignment and hyphal growth unit, with a principal component analysis performed in GraphPad Prism v. 10. Confocal imaging was performed on Nile Blue-tagged samples from the sample surface and reconstructed using Imaris. LOX and NF-κB staining on DECIPHER and native tissue samples were quantified for their co-localization with collagen (CNA35) using Fiji JaCoP macro[67]. ICC samples stained with α-SMA, integrin α_5, LOX, p53, TIMP3 and F-actin were analysed with CellProfiler for intensity and morphological metrics. Nucleus/cytosol localization ratio of YAP was quantified using CellProfiler (v.4.2.5) by identifying the fluorescence from a 30-pixel perinuclear ring as the cytosolic localization. Paxillin quantification was performed using a custom Fiji script in which focal adhesion sites were identified using auto local threshold (Bernsen) followed by particle analysis.

Bioinformatics analysis

For mass spectrometry data, the raw reads were obtained with FDR ≤ 1% and quantitative analysis was performed based on the peak intensity, peak area and liquid chromatography retention time of the samples, followed by a series of statistical analysis and quality control. The protein identification results were based on UniProt Protein Database (*Mus musculus*). Subsequent bioinformatics analysis and data visualization were processed using BGI's Dr. Tom online analysis platform. Additional data visualization was performed using OriginPro 2024 and TBtools[68].

RNA-seq reads were aligned to the mouse genome assembly mm39 (BioProject no. PRJNA20689) with STAR (v.2.7.8a). The aligned reads were quantified using HTSeq (0.11.0) with Ensembl transcripts release 105. The above computation was performed within the PartekFlow cloud environment with default parameters (v.10.0.23.0425). DEG analysis was done with the DESeq2 package[69] (Bioconductor 3.17) and clusterProfiler package[70,71] (Bioconductor 3.17) was used to perform the functional enrichment analysis. Cellinker[31] was used to correlate the ligand–receptor interaction between ECM proteomics and CF RNA. Data visualization was performed using OriginPro 2024, GraphPad Prism 9, MATLAB R2023a and TBtools[68].

Statistics and reproducibility

No statistical method was used to predetermine the sample size. Sample sizes were determined based on previous studies in similar fields. Unless otherwise noted, all the experiments were performed as triplicate independent experiments ($N \geq 3$). Detailed sample sizes can be found in the respective figure captions. The number of cells analysed are reported in each figure with individual data points as well as in Supplementary Table 4. Data are expressed as the mean ± standard deviation (s.d.) or standard error of the mean (s.e.m.), with the sample size and applied statistical analysis specified in each figure caption. Statistical analyses were performed using GraphPad Prism v. 9 and v. 10. All the box graphs shown in the figures have the box range showing the interquartile data, centre of the box represents the median, '+' mark represents the mean, and whiskers represent the minimum and maximum values. Representative IHC and ICC images shown in this study were successfully reproduced with similar results in three independent attempts. Other representative micrographs, such as Figs. 1c and 2a,b, were successfully reproduced with similar results for more than ten times throughout this study. No data were excluded from the analyses. In vitro experiments and samples used were randomly allocated. The investigators were blinded during data collection but not blinded during outcome assessment because the analyses were done objectively with automated scripts and codes.

Heat maps demonstrating the DEG analysis in the RNA-seq data were graphed by averaging the replicates, with the original (unaveraged) readings and dendrograms shown in Extended Data Fig. 4 (except in Fig. 3b where the original data are shown). The heat map in Fig. 3j is shown following the order of the other DEG heat maps, with the original clustering dendrogram shown in Extended Data Fig. 4a. The gene expression results for the DECIPHER samples are normalized to the young and aged groups of their respective in vivo mimic, that is, young CFs are normalized to the young ECM in a soft matrix (young CFs

on SoftY), whereas aged CFs are normalized to the aged ECM in a stiff matrix (aged CFs on StiffA). The Ct (cycle threshold) values of RT-qPCR results were obtained via Bio-Rad CFX Maestro software (v.2.3) and analysed by the $2^{-\Delta\Delta Ct}$ method[72] against glyceraldehyde 3-phosphate dehydrogenase and the aforementioned in vivo mimic groups.

Reporting summary

Further information on research design is available in the Nature Portfolio Reporting Summary linked to this article.

Data availability

The data supporting the findings of this study are available within the article and its Supplementary Information. Raw images are available from the corresponding author upon request due to large file sizes. The mass spectrometry proteomics data have been deposited in the ProteomeXchange Consortium in the PRIDE repository with dataset identifier PXD060864. The RNA-seq data have been deposited in the NCBI GEO repository with accession code GSE289885. Source data are provided with this paper.

Code availability

All codes and scripts newly written in this study can be accessed via Zenodo at https://doi.org/10.5281/zenodo.15080541 (ref. 73) and via GitHub at https://github.com/onghuiting/focal_adhesion_analysis.

References

64. Hwang, J. et al. Molecular assessment of collagen denaturation in decellularized tissues using a collagen hybridizing peptide. *Acta Biomater.* **53**, 268–278 (2017).
65. Aper, S. J. A. et al. Colorful protein-based fluorescent probes for collagen imaging. *PLoS ONE* **9**, e114983 (2014).
66. Ackers-Johnson, M. & Foo, R. S. Langendorff-free isolation and propagation of adult mouse cardiomyocytes. *Methods Mol. Biol.* **1940**, 193–204 (2019).
67. Bolte, S. & Cordelières, F. P. A guided tour into subcellular colocalization analysis in light microscopy. *J. Microsc.* **224**, 213–232 (2006).
68. Chen, C. et al. TBtools: an integrative toolkit developed for interactive analyses of big biological data. *Mol. Plant* **13**, 1194–1202 (2020).
69. Love, M. I., Huber, W. & Anders, S. Moderated estimation of fold change and dispersion for RNA-seq data with DESeq2. *Genome Biol.* **15**, 550 (2014).
70. Wu, T. et al. clusterProfiler 4.0: a universal enrichment tool for interpreting omics data. *Innovation* **2**, 100141 (2021).
71. Yu, G., Wang, L.-G., Han, Y. & He, Q.-Y. clusterProfiler: an R package for comparing biological themes among gene clusters. *OMICS* **16**, 284–287 (2012).
72. Livak, K. J. & Schmittgen, T. D. Analysis of relative gene expression data using real-time quantitative PCR and the 2−ΔΔCT method. *Methods* **25**, 402–408 (2001).
73. Ting, O. H. Hybrid hydrogel-extracellular matrix scaffolds identify biochemical and mechanical signatures of cardiac aging. *Zenodo* https://doi.org/10.5281/zenodo.15080541 (2025).

Acknowledgements

We thank J. Marlena (Mechanobiology Institute (MBI), National University of Singapore (NUS)) for illustrations; C. J. Chan, V. Prabhakaran and B. H. Ng (MBI, NUS) for providing hyaluronan binding protein and vibratome for usage; R. Li, A. Holle, J. Yan, H. H. Susapto, H. T. Ong, R. D. Mets, R. M. Hengst, X. Gao, Y. Li, J. P. Singh (MBI, NUS), J. J. Zhou (Electrical and Computer Engineering, NUS) and C. Mellace (Optics11 Life) for fruitful discussions and technical advice; H. T. Ong (MBI, NUS) for image analysis codes; X. Zhang (Department of Biological Sciences, NUS) for assistance with optimizing the AFM experiments; and T. Luu (Cardiovascular Research Institute, National University Health System) for assistance with animal handling. We thank the MBI Wet Lab Core for facility and technical support, the Singapore Microscopy and Bioimaging Analysis (SiMBA, MBI) core for microscopy and data processing facilities and the High-throughput Molecular Genetics (HMG, MBI) core for RNA-seq support. This work was supported by the Ministry of Education under the Research Centres of Excellence programme through the Mechanobiology Institute at the National University of Singapore and the Biomedical Engineering Department at the National University of Singapore, as well as the Singapore Ministry of Education Academic Research Fund Tier 3 (MOE grant no. MOET32021-0003) to J.L.Y.

Author contributions

J.L.Y. and A.R.S. conceptualized the project and wrote the paper. J.L.Y. supervised the data collection and analysis. A.R.S. performed majority of the experiments and data analysis. M.F.H.R., X.S. and D.C. assisted in the bench experiments related to ECM staining, imaging and data analysis. X.S. assisted in tissue harvesting and mice handling. K.K.R. and Y.L. performed the correlative confocal–AFM experiments. Y.H., P.V. and M.A.-J. contributed to the revision experiments (not included in the paper). M.A.-J. performed the primary cell isolations. J.Z. assisted in the RNA-seq experiments and analysis. R.S.F. provided the key reagents and contributed to the discussion.

Competing interests

The authors declare no competing interests.

Additional information

Extended data is available for this paper at https://doi.org/10.1038/s41563-025-02234-6.

Supplementary information The online version contains supplementary material available at https://doi.org/10.1038/s41563-025-02234-6.

Correspondence and requests for materials should be addressed to Jennifer L. Young.

Peer review information *Nature Materials* thanks Feng Zhao and the other, anonymous, reviewer(s) for their contribution to the peer review of this work.

https://doi.org/10.1038/s41563-025-02234-6

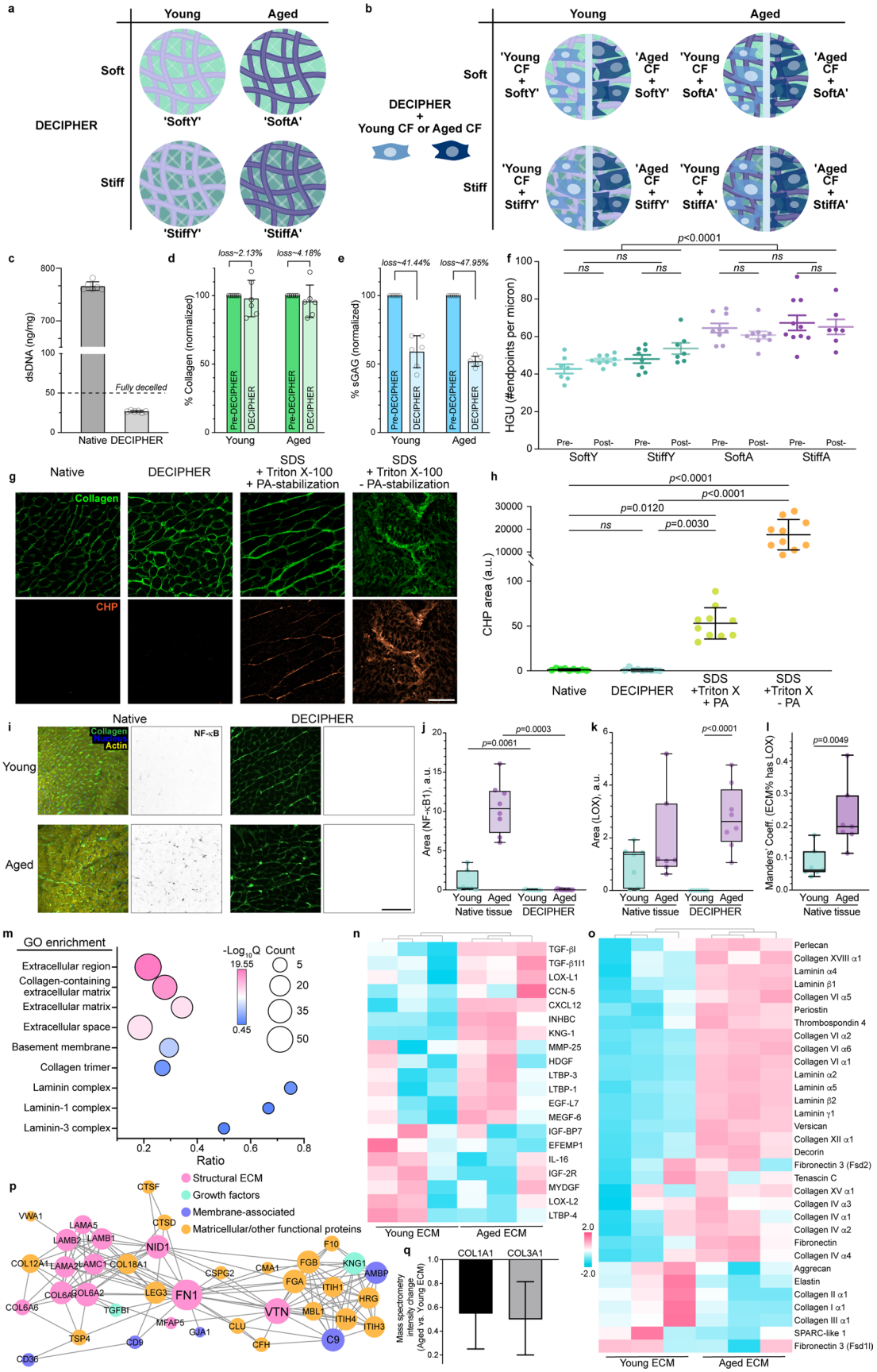

Extended Data Fig. 1 | See next page for caption.

https://doi.org/10.1038/s41563-025-02234-6

Extended Data Fig. 1 | Characterization of DECIPHER samples. Nomenclatures used in this study describing DECIPHER samples before (**a**) and after cell seeding (**b**). Assay for dsDNA content in native tissue ('Native') vs. DECIPHER samples, with the accepted decellularization threshold of 50 ng/mg indicated by the dashed line (**c**). Hydroxyproline (collagen) content (**d**), and sGAG content (**e**) in Pre-DECIPHER vs. DECIPHER samples. The number of endpoints per micron (hyphal growth factor, HGU) is the most age-regulated ECM architectural factor identified by TWOMBLI (**f**). IHC images of collagen hybridizing peptide (CHP) and collagen stained samples of Pre-DECIPHER, DECIPHER, SDS + Triton X-100 +/− PA stabilization (**g**), quantified in (**h**). IHC staining of intracellular transcription factor NF-kB1 (**i**) and quantified in (**j**) as negative control for LOX area (**k**) and localization (**l**) quantification. Gene ontology (GO) enrichment analysis of ECM mass spectrometry data, where bubble size indicates number of DEPs in each set and color bar indicates adjusted significance by Q-value (**m**). Highlighted matrix-immobilized molecules (**n**) and ECM proteins (**o**) quantified by mass spectrometry. Protein-protein interaction (PPI) analysis of differentially expressed proteins (**p**). Collagen I/III ratio increased 9.4% in aged cardiac ECM calculated from mass spectrometry intensity using propagation of uncertainty (**q**). Color bar indicates row-standardized expression (**n**, **o**). Data are mean ±SD (**c**-**f**, **h**, **q**). N = 3 biological replicates for each condition in (**c**-**o**). One-way ANOVA with Dunn's multiple comparison (**h**, **j**, **k**), unpaired two-tailed t-test (l). ns, not significant ($p > 0.05$). Scale bar: 50 µm (**g**), 100 µm (i).

https://doi.org/10.1038/s41563-025-02234-6

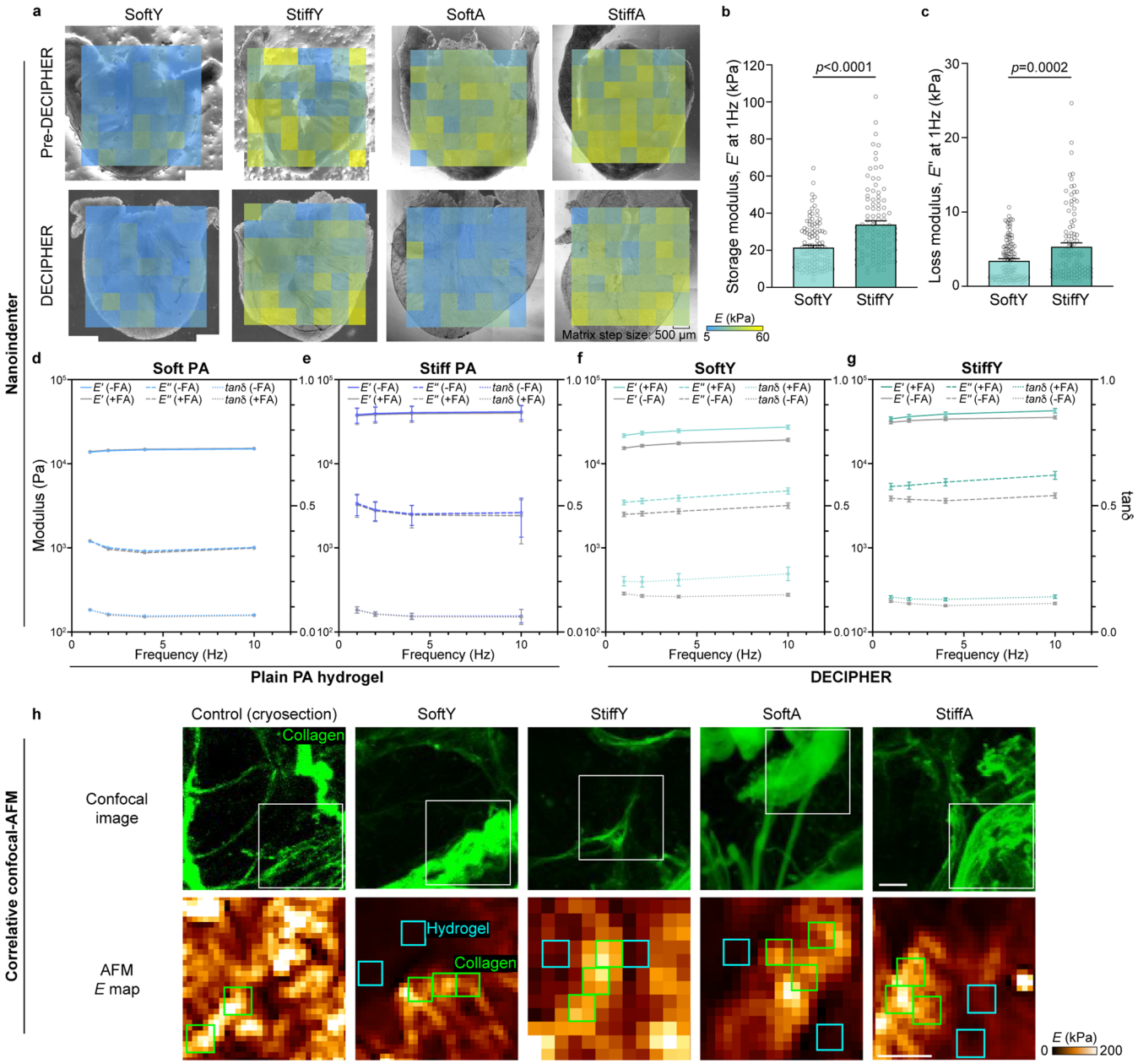

Extended Data Fig. 2 | Stiffness mapping of pre- and post-DECIPHER samples reveals scaffold tunability. Nanoindentation maps of Pre-DECIPHER and DECIPHER samples of young (Y) and aged (A) tissue with soft or stiff hydrogel component (**a**). Storage (**b**) and loss (**c**) moduli of DECIPHER samples at 1 Hz oscillation measured by dynamic mechanical analysis. Storage modulus, loss modulus, and tanδ of plain soft (**d**) or stiff PA hydrogel (**e**), as well as SoftY (**f**) or StiffY (**g**) DECIPHER samples fabricated with or without formaldehyde (+FA or -FA, respectively). Examples of correlative confocal-atomic force microscopy maps for tissue ('Control (cryosection)') and DECIPHER samples (**h**). Top row images are maximum intensity projections (MIPs) of the confocal stacks live stained with CNA35 (collagen). Bottom row images are AFM stiffness (E, kPa) maps. Quantified regions of interests (hydrogel vs. collagen regions) from the AFM maps are indicated. N = 3 (**b**-**g**) or 2 (**h**) biological replicates for each condition. StiffY image is a zoomed-in version of Fig. 2j. Scale bar: 5 µm (**h**).

https://doi.org/10.1038/s41563-025-02234-6

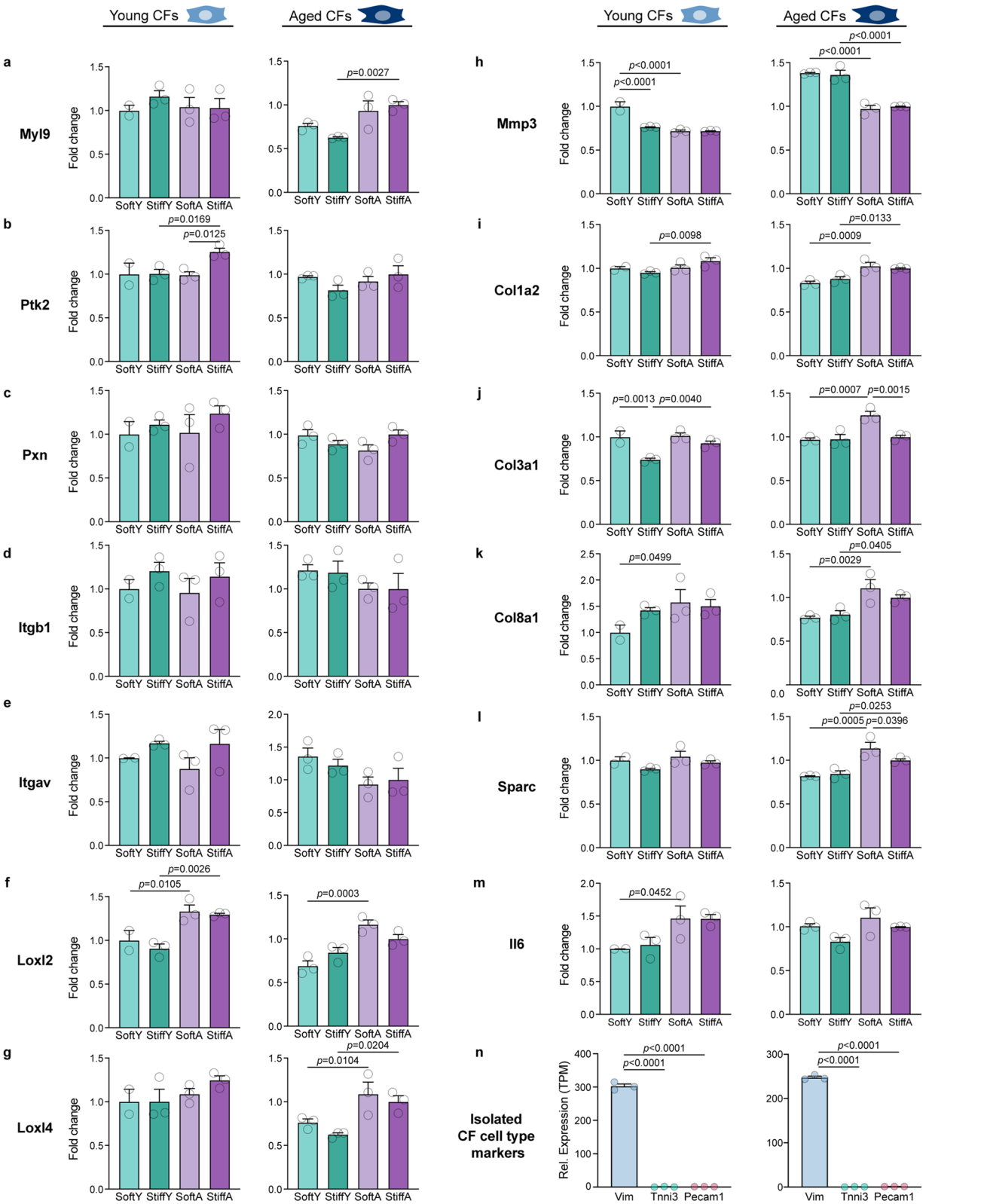

Extended Data Fig. 3 | Additional CF gene expression levels quantified by RNA-seq. Normalized gene expression on different DECIPHER samples (SoftY, StiffY, SoftA, StiffA). Quantified RNA-seq data for genes regulating young or aged CF activation (**a**), mechanosensing (**b, c, d, e**), ECM remodeling (**f, g, h, i, j, k, l**), and senescence (**m**). Specificity analysis of primary CF isolation reveals a pure vimentin-expressing (Vim) CF population with negligible CD31-expressing (Pecam1) endothelial cells and troponin-I-expressing (Tnni3) cardiomyocytes (**n**). N = 3 biological replicates for each condition, except Young CF+SoftY group in RNA-seq (N = 2). Data are mean ±SEM (**a**-**n**). One-way ANOVA with Fisher's preplanned multiple comparison (each pair with one variable, ECM or stiffness, **a**-**n**).

https://doi.org/10.1038/s41563-025-02234-6

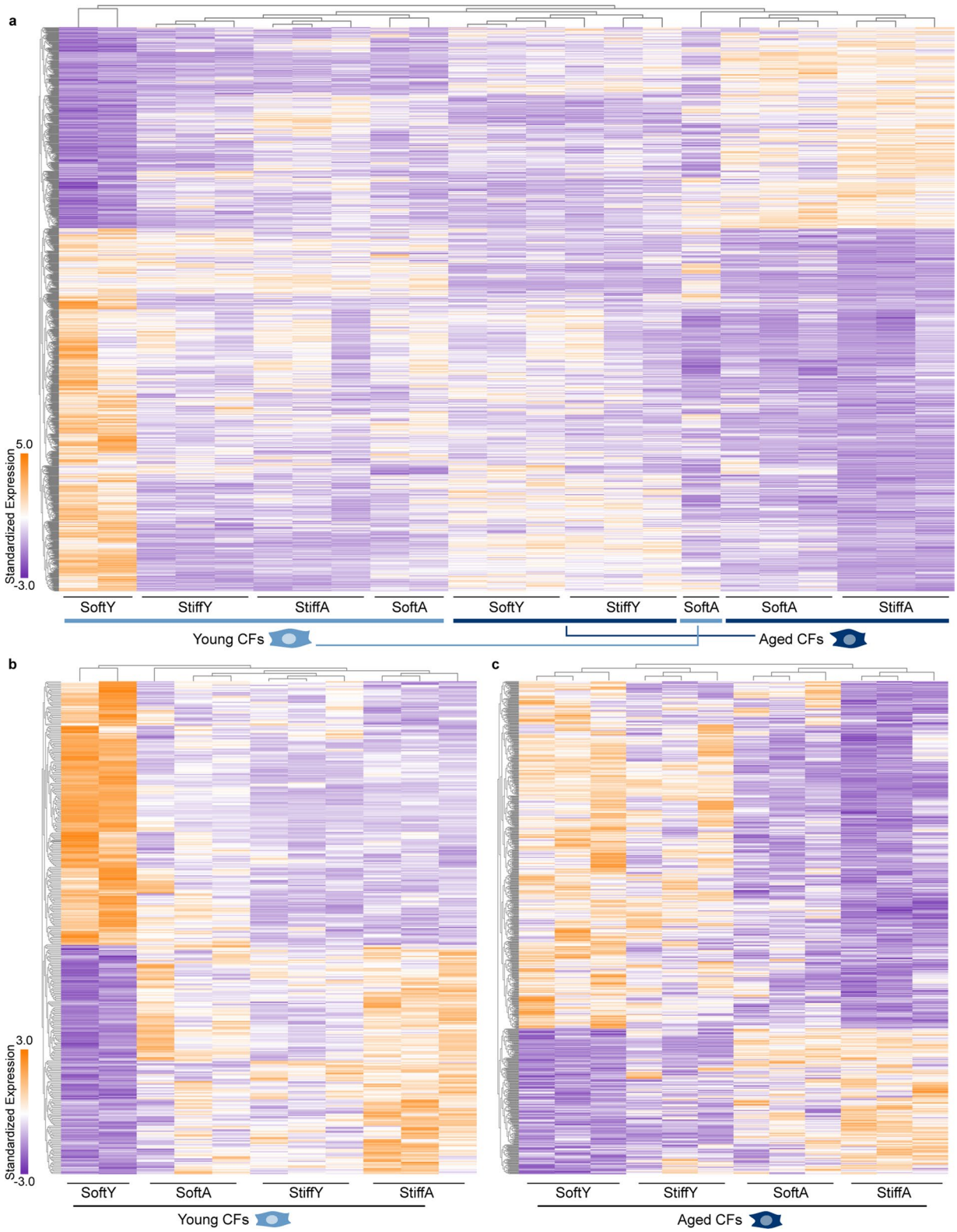

Extended Data Fig. 4 | CF activation/quiescence and aging/rejuvenation-like phenotypes shown by original DEG heatmaps with dendrograms. Sample replicates are non-averaged in this graph set, where **a**, **b**, **c** correspond to Figs. 3j, 6a and b, respectively. DEGs are FC > 1.5 or < 2/3 and $p < 0.05$ (Wald test with Benjamini-Hochberg correction). Color bar indicates row-standardized expression.

https://doi.org/10.1038/s41563-025-02234-6

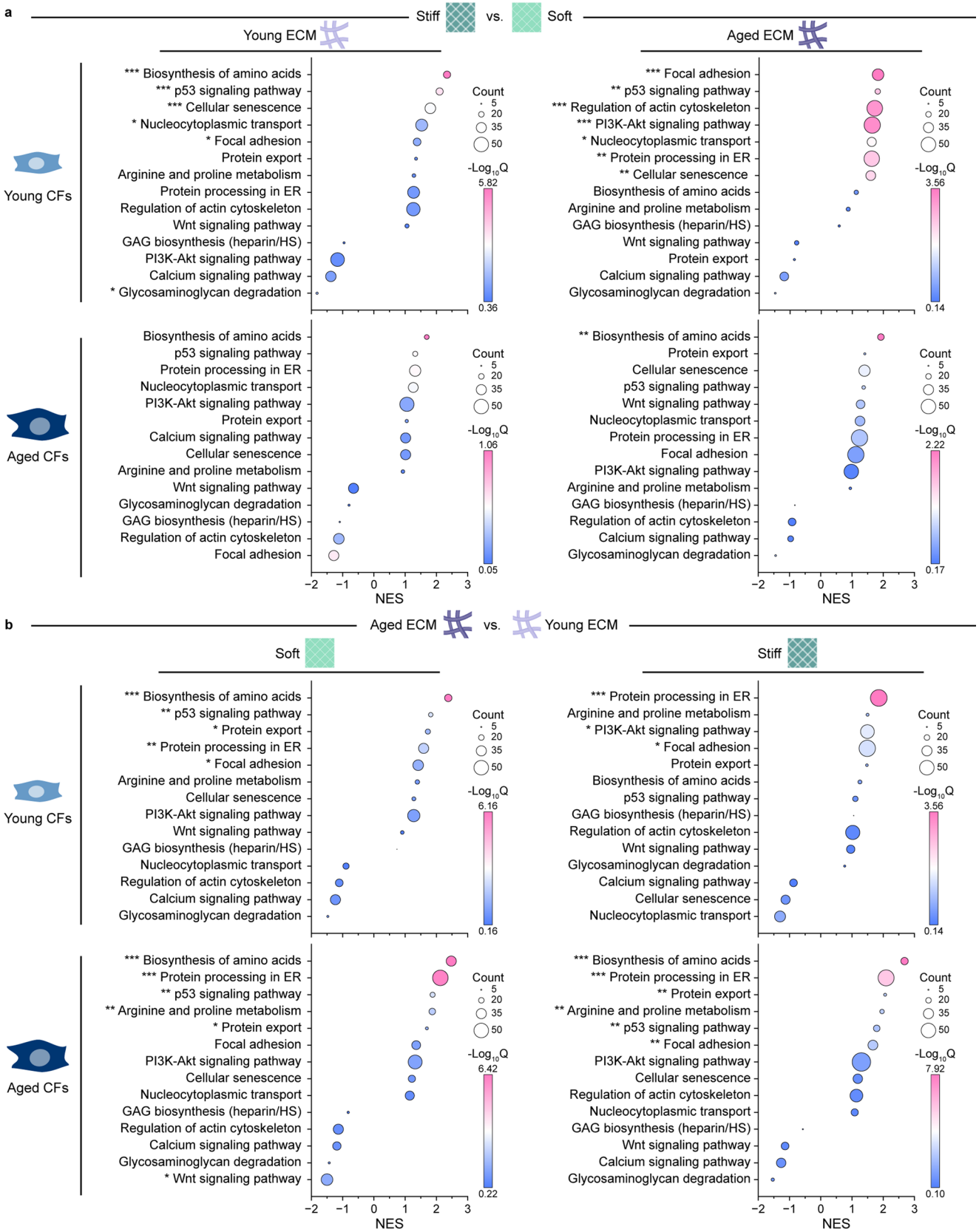

Extended Data Fig. 5 | KEGG enrichment analysis of CFs seeded on DECIPHER samples. Highlighted pathways of interest in young or aged CFs impacted by mechanical cues (Stiff vs. Soft, **a**) or ECM aging (Aged ECM vs. Young ECM, **b**) were graphed in the order of normalized enrichment score (NES) with color bar showing adjusted significance using Q-value (Two-sided Benjamini-Hochberg test). Significantly regulated pathways were marked with asterisks beside the pathway name: *Q < 0.05, **Q < 0.01, ***Q < 0.001. Bubble size indicates the number of genes differentially expressed in each pathway set.

https://doi.org/10.1038/s41563-025-02234-6

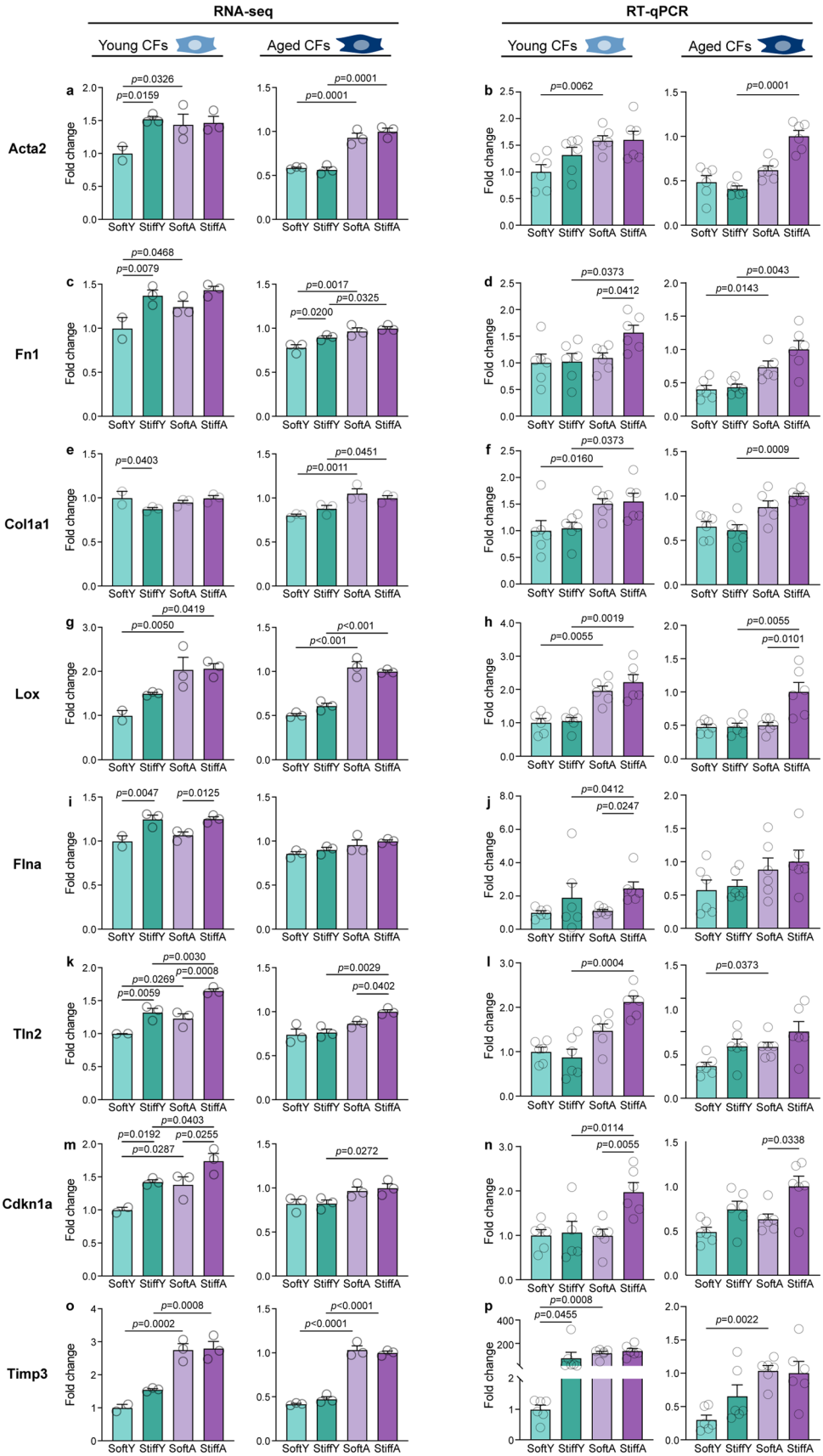

Extended Data Fig. 6 | RT-qPCR validation of gene expression compared to RNA-seq. Normalized gene expression on different DECIPHER samples (SoftY, StiffY, SoftA, StiffA). Fold changes in RT-qPCR results (**b**, **d**, **f**, **h**, **j**, **l**, **n**, **p**) were calculated using $2^{-\Delta\Delta Ct}$ method and compared side-by-side with RNA-seq results (**a**, **c**, **e**, **g**, **i**, **k**, **m**, **o**). N = 3 biological replicates for each condition, except Young CF+SoftY group in RNA-seq (N = 2). Data are mean ±SEM (**a**-**p**). One-way ANOVA with Fisher's preplanned multiple comparison (each pair with one variable, ECM or stiffness, **a**-**p**).

https://doi.org/10.1038/s41563-025-02234-6

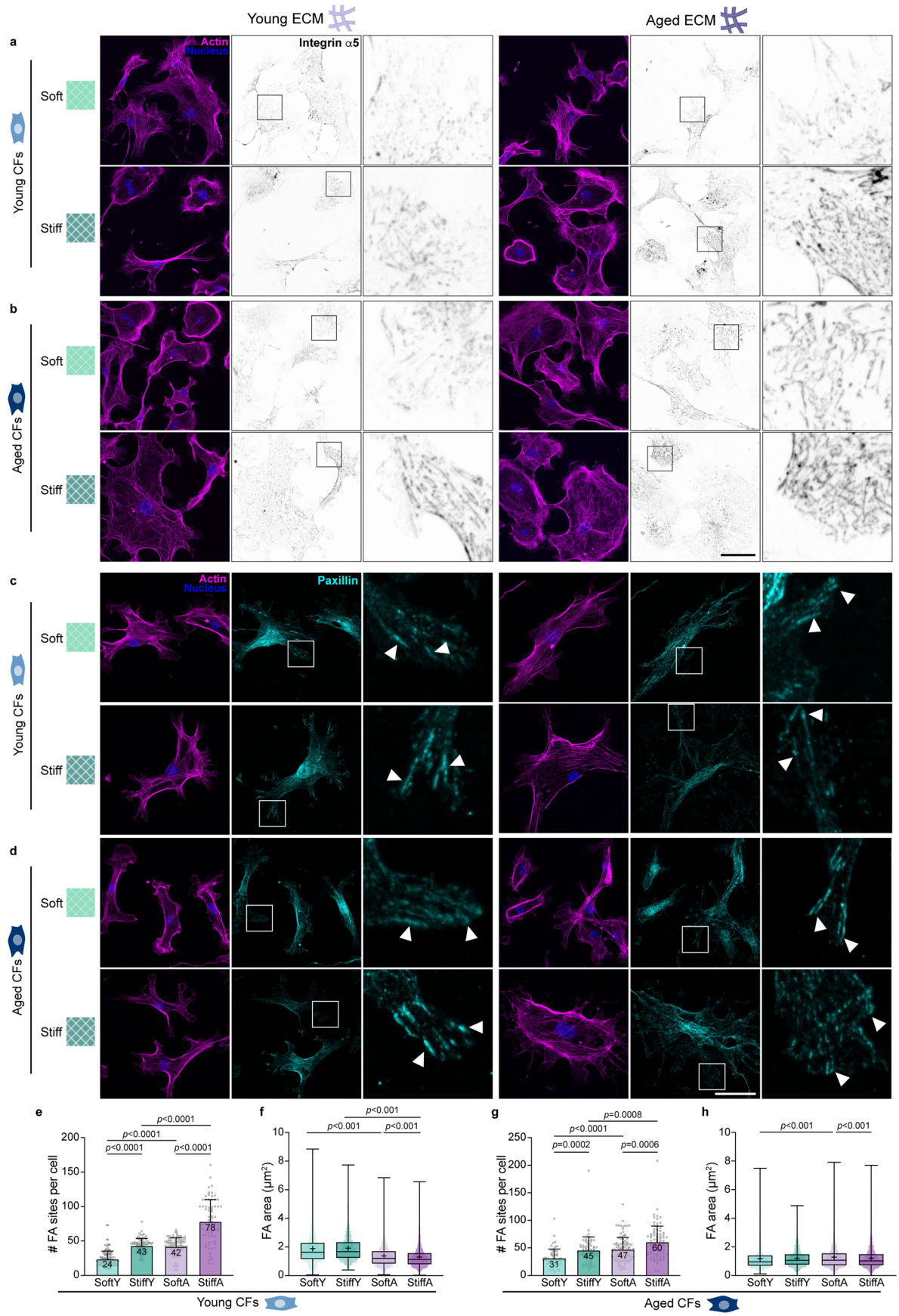

Extended Data Fig. 7 | See next page for caption.

https://doi.org/10.1038/s41563-025-02234-6

Extended Data Fig. 7 | Integrin and focal adhesion formation on DECIPHER scaffolds. ICC of F-actin, nucleus, α_5 integrin, and paxillin in young CFs (**a**, **c**) and aged CFs (**b**, **d**) on DECIPHER samples (SoftY, StiffY, SoftA, or StiffA). α_5 integrin insets are indicated by the black boxes, paxillin insets are indicated by the white boxes, and white arrows point to focal adhesions. The number and area of focal adhesion sites in young CFs (**e**, **f**) and aged CFs (**g**, **h**) quantified from paxillin staining. N = 3 biological replicates for each condition (**e**-**h**). Data are mean ±SD (**e**, **g**). One-way ANOVA with Fisher's preplanned multiple comparison (each pair with one variable, ECM or stiffness, **e**-**h**). Scale bar: 50 μm.

https://doi.org/10.1038/s41563-025-02234-6

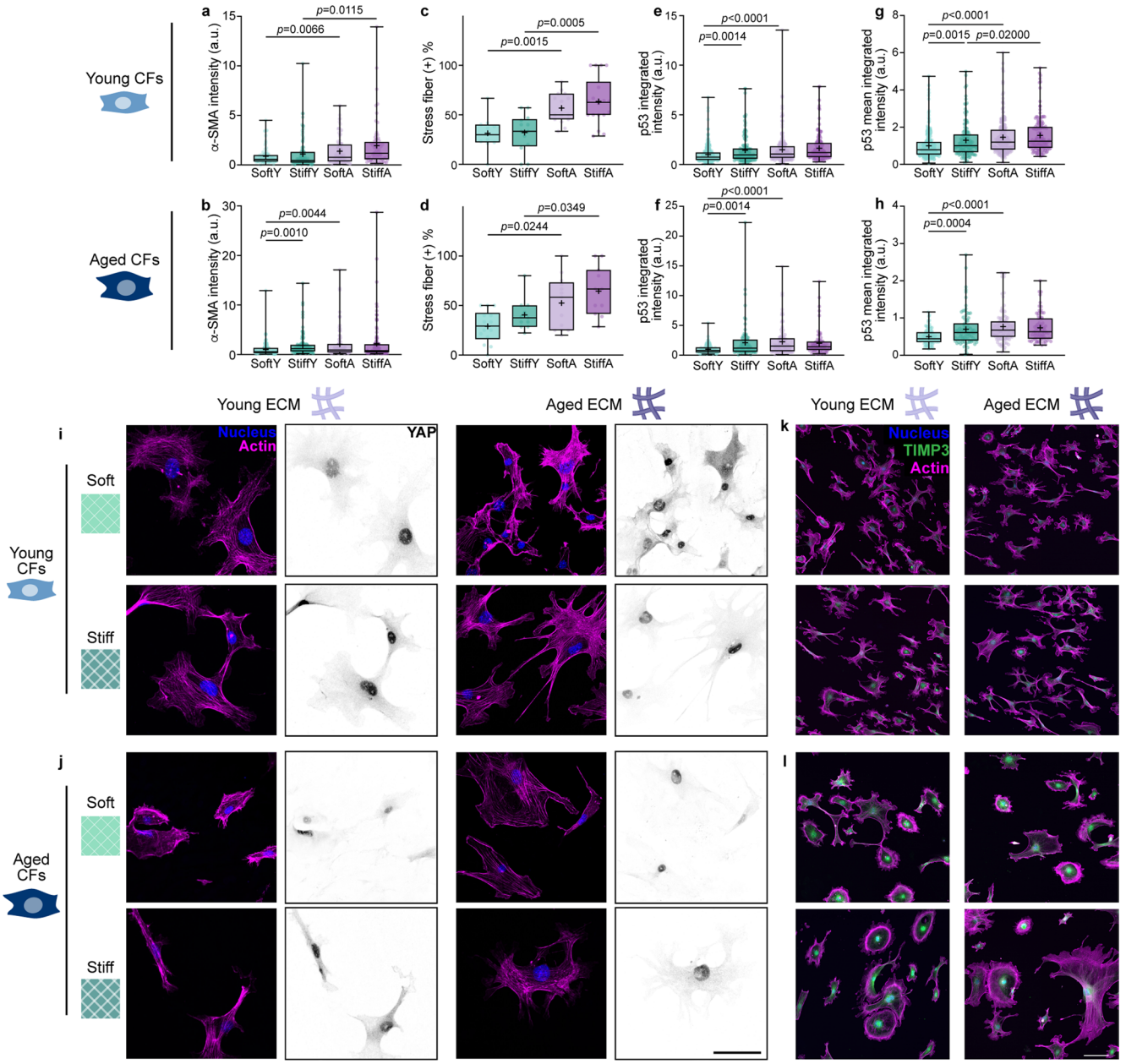

Extended Data Fig. 8 | ECM ligands and mechanics dictate CF activation, mechanosensitive, and senescence phenotypes. ICC images shown in Fig. 4j and k were quantified for α-SMA intensity and stress fiber assembly for young CFs (**a**, **c**) and aged CFs (**b**, **d**). ICC images shown in Fig. 6l and m were quantified for p53 integrated intensity and mean intensity for young CFs (**e**, **g**) and aged CFs (**f**, **h**). ICC images of young (**i**) and aged CFs (**j**) on DECIPHER samples stained for nucleus, F-actin, YAP (**i**, **j**), and TIMP3 (**k**, **l**). SoftY and StiffA TIMP3 images are also shown in Fig. 6k. One-way ANOVA with Fisher's preplanned multiple comparison (each pair with one variable, ECM or stiffness) was used for (**a**-**h**), N = 3 biological replicates for each condition. Scale bar: 50 μm (**i**, **j**), 100 μm (**k**, **l**).

https://doi.org/10.1038/s41563-025-02234-6

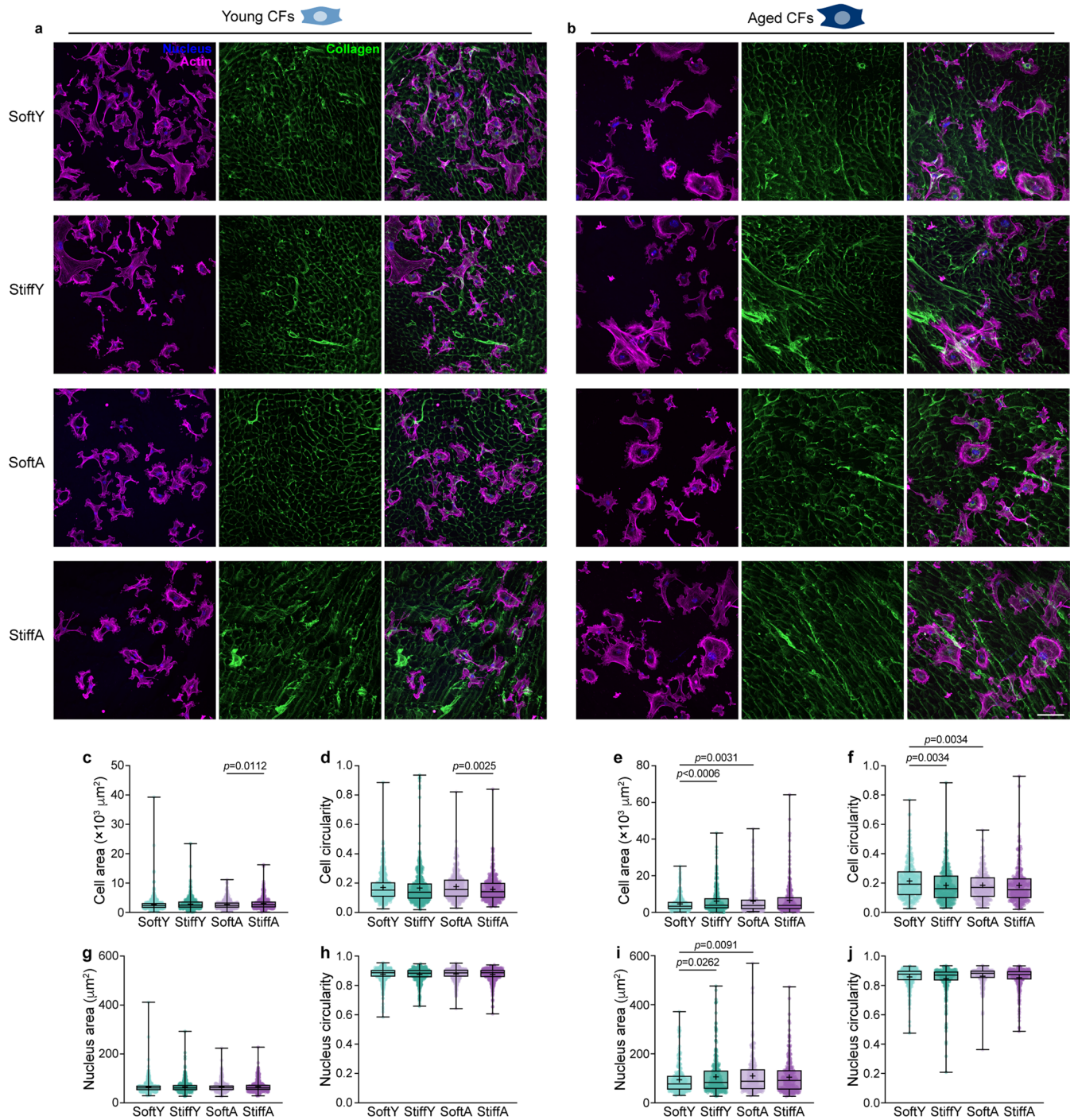

Extended Data Fig. 9 | Morphological changes in CFs are governed by stiffness. Low magnification images of young and aged CFs cultured on DECIPHER samples immunostained for F-actin, nucleus, and collagen (**a, b**). Cell morphology (area and circularity) of young CFs (**c, d**) and aged CFs (**e, f**), as well as nuclear morphology (area and circularity) of young CFs (**g, h**) and aged CFs (**i, j**) on DECIPHER samples. One-way ANOVA with Fisher's preplanned multiple comparison (each pair with one variable, ECM or stiffness) was used for (**e**-**h**), N = 12 biological replicates for each condition. Scale bar: 100 μm.

https://doi.org/10.1038/s41563-025-02234-6

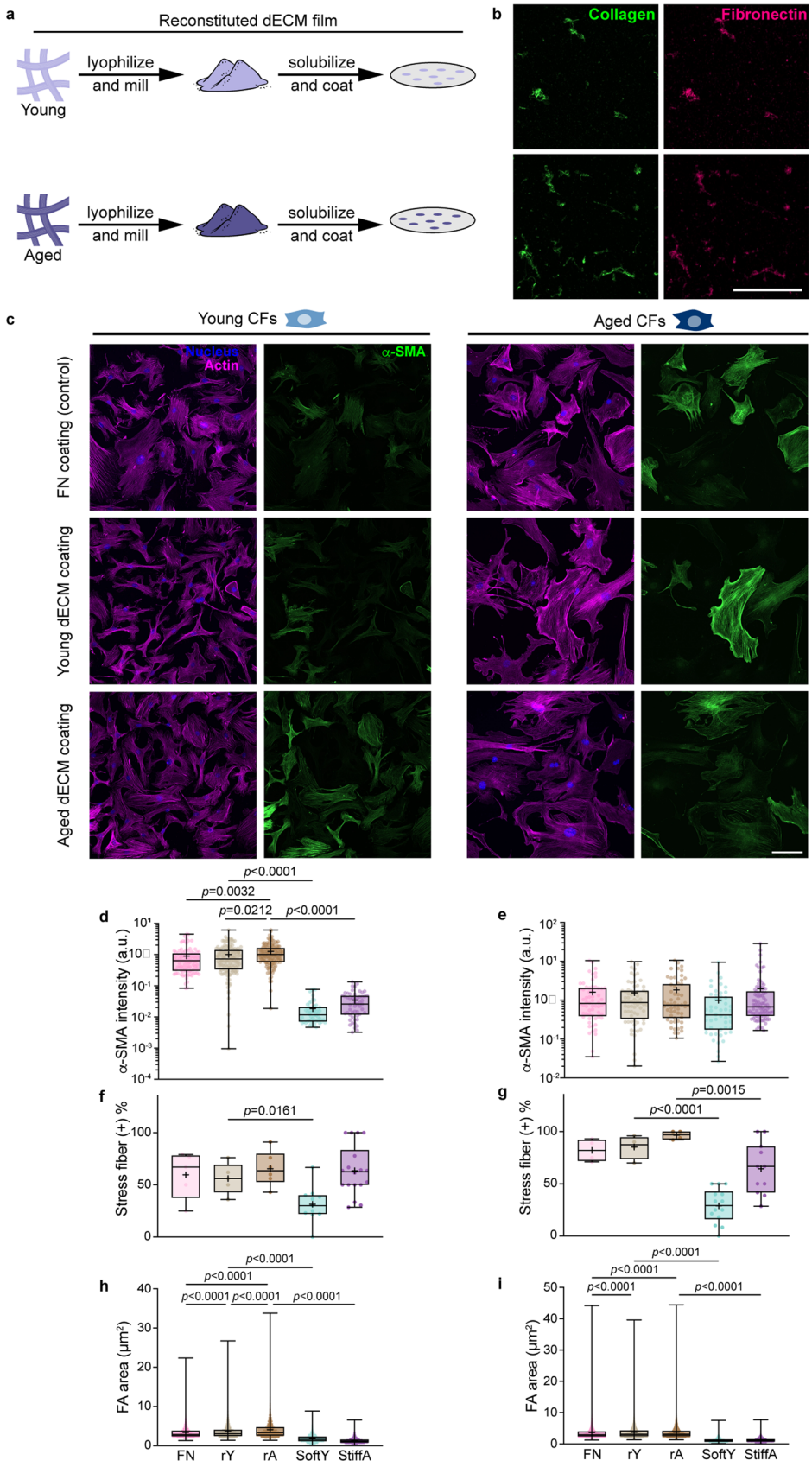

Extended Data Fig. 10 | Conventional reconstituted dECM films do not recapitulate native tissue properties. Decellularized young or aged ECM were lyophilized, pulverized, and solubilized prior to coverslip coating (**a**). Immunostaining shows fragmented reconstituted dECM and a destruction of native architecture (**b**) compared to native tissue or DECIPHER materials (shown in Fig. 2a, **b**). Young or aged CFs were seeded onto dECM films (with control coating fibronectin, FN) and immunostained for nucleus, F-actin, and α-SMA(**c**). CF activation and focal adhesion formation were quantified for young (**d**, **f**, **h**) and aged CFs (**e**, **g**, **i**) and compared with DECIPHER data (SoftY and StiffA). N = 3 samples for each condition. One-way ANOVA with Fisher's preplanned multiple comparison (each pair with one variable, ECM or stiffness, **d**-**i**). Scale bar: 50 μm (**b**), 100 μm (**c**).

nature portfolio

Corresponding author(s): Jennifer L Young

Last updated by author(s): Feb 24, 2025

Reporting Summary

Nature Portfolio wishes to improve the reproducibility of the work that we publish. This form provides structure for consistency and transparency in reporting. For further information on Nature Portfolio policies, see our Editorial Policies and the Editorial Policy Checklist.

Statistics

For all statistical analyses, confirm that the following items are present in the figure legend, table legend, main text, or Methods section.

n/a	Confirmed	
☐	☒	The exact sample size (*n*) for each experimental group/condition, given as a discrete number and unit of measurement
☐	☒	A statement on whether measurements were taken from distinct samples or whether the same sample was measured repeatedly
☐	☒	The statistical test(s) used AND whether they are one- or two-sided *Only common tests should be described solely by name; describe more complex techniques in the Methods section.*
☒	☐	A description of all covariates tested
☐	☒	A description of any assumptions or corrections, such as tests of normality and adjustment for multiple comparisons
☐	☒	A full description of the statistical parameters including central tendency (e.g. means) or other basic estimates (e.g. regression coefficient) AND variation (e.g. standard deviation) or associated estimates of uncertainty (e.g. confidence intervals)
☐	☒	For null hypothesis testing, the test statistic (e.g. *F*, *t*, *r*) with confidence intervals, effect sizes, degrees of freedom and *P* value noted *Give P values as exact values whenever suitable.*
☒	☐	For Bayesian analysis, information on the choice of priors and Markov chain Monte Carlo settings
☒	☐	For hierarchical and complex designs, identification of the appropriate level for tests and full reporting of outcomes
☒	☐	Estimates of effect sizes (e.g. Cohen's *d*, Pearson's *r*), indicating how they were calculated

Our web collection on statistics for biologists contains articles on many of the points above.

Software and code

Policy information about availability of computer code

Data collection	Confocal imaging data were collected using Nikon A1R scanning laser confocal microscope with NIS-Elements software (v5.30.05) or Oxford Instruments BC43 spinning disk confocal microscope with Fusion software (v2.3). Fluorescence and absorption-based quantifications were read using a Promega GloMax plate reader. Young's modulus and dynamic mechanical analysis (DMA) data were collected using Optics11 Chiaro Nanoindenter with Optics11Life software. Correlative confocal-atomic force microscope data were collected using a JPK NanoWizard 4 XP Bioscience AFM system with a BioMAT Workstation (Bruker) was used in conjunction with an upright Stellaris 8 laser scanning confocal microscope (Leica). Scanning electron microscopy images were obtained using a Hitachi Regulus 8230 system. RNA sequencing was performed using an Illumina NovaSeq 6000 system. Multiplex reverse transcription quantitative PCR (RT-qPCR) data were collected using Bio-Rad CFX96 detection system. TMT-based quantitative mass spectrometry data were collected using Thermo Scientific Q-Exactive HF X Mass Spectrometer connected to a Thermo ScientificTM UltiMateTM 3000 UHPLC system.
Data analysis	ImageJ/FIJI 1.53t, CellProfiler 4.2.4, OriginPro 2024a, Imaris 10, GraphPad Prism 9 and 10, MATLAB R2024a, Optics11Life DataViewer, JPK data analysis software (v8.0.144), Bioconductor 3.17, STAR (2.7.8a), HTSeq (0.11.0), Bio-Rad CFX Maestro, BGI Dr. Tom platform, and TBTools v1.120 were used for data analysis. Custom codes are available via GitHub (https://github.com/onghuiting/focal_adhesion_analysis).

For manuscripts utilizing custom algorithms or software that are central to the research but not yet described in published literature, software must be made available to editors and reviewers. We strongly encourage code deposition in a community repository (e.g. GitHub). See the Nature Portfolio guidelines for submitting code & software for further information.

Data

Policy information about availability of data

All manuscripts must include a data availability statement. This statement should provide the following information, where applicable:

- Accession codes, unique identifiers, or web links for publicly available datasets
- A description of any restrictions on data availability
- For clinical datasets or third party data, please ensure that the statement adheres to our policy

The data supporting the findings of this study are available within the article and supplementary materials. Raw images are available from the corresponding author upon request due to large file sizes. The mass spectrometry proteomics data have been deposited to the ProteomeXchange Consortium via the PRIDE repository with the dataset identifier PXD060864. The RNA-seq data have been deposited to NCBI GEO repository with accession code GSE289885, and mouse genome assembly mm39 is from BioProject #PRJNA20689.

Research involving human participants, their data, or biological material

Policy information about studies with human participants or human data. See also policy information about sex, gender (identity/presentation), and sexual orientation and race, ethnicity and racism.

Reporting on sex and gender	N/A
Reporting on race, ethnicity, or other socially relevant groupings	N/A
Population characteristics	N/A
Recruitment	N/A
Ethics oversight	N/A

Note that full information on the approval of the study protocol must also be provided in the manuscript.

Field-specific reporting

Please select the one below that is the best fit for your research. If you are not sure, read the appropriate sections before making your selection.

☒ Life sciences ☐ Behavioural & social sciences ☐ Ecological, evolutionary & environmental sciences

For a reference copy of the document with all sections, see nature.com/documents/nr-reporting-summary-flat.pdf

Life sciences study design

All studies must disclose on these points even when the disclosure is negative.

Sample size	No statistical method was used to predetermine sample size. Sample sizes were determined based on previous studies in similar fields. Unless otherwise noted, all experiments were performed as triplicate independent experiments (n ≥ 3). Detailed sample sizes can be found in respective figure captions. The number of cells analyzed are reported in each figure with individual data points and in Supplementary Table 4.
Data exclusions	In RNA sequencing preparation, one replicate sample (YCF_SoftY-02) was excluded due to low RNA quality (RIN<8.5). The sample was discarded before amplification and sequencing. No data were excluded in any experiments.
Replication	Unless otherwise noted, all experiments were performed as triplicate independent experiments (n ≥ 3). All attempts to reproduce our findings were successful.
Randomization	In hydrogel/DECIPHER sample fabrication and characterization, solutions used were prepared in different batches. Samples were randomly prepared and allocated in each group. For each in vitro studies, n = 3-6 young hearts and n = 3-4 aged hearts were used to fabricate DECIPHER samples. CFs used in this study were isolated from n = 3 young hearts and n = 2 aged hearts and randomly seeded to biologically replicated DECIPHER samples. Imaging was done with multiple fields randomly selected.
Blinding	The investigators were blinded during data collection but not blinded during outcome assessment because analyses were done objectively with automated scripts and codes. During confocal imaging, researchers were blinded by turning off the laser channel of interest and randomly selecting imaging region using another channel (e.g., nucleus). For RNA-seq preparation and sequencing experiments, researchers were blinded (samples were arranged in 96 well plate coordinates by an alternative person so that the researcher carrying out the experiments is not aware of group specifications).

Reporting for specific materials, systems and methods

We require information from authors about some types of materials, experimental systems and methods used in many studies. Here, indicate whether each material, system or method listed is relevant to your study. If you are not sure if a list item applies to your research, read the appropriate section before selecting a response.

Materials & experimental systems

n/a	Involved in the study
☐	☒ Antibodies
☒	☐ Eukaryotic cell lines
☒	☐ Palaeontology and archaeology
☐	☒ Animals and other organisms
☒	☐ Clinical data
☒	☐ Dual use research of concern
☒	☐ Plants

Methods

n/a	Involved in the study
☒	☐ ChIP-seq
☒	☐ Flow cytometry
☒	☐ MRI-based neuroimaging

Antibodies

Antibodies used

Collagen (CNA35 collagen binding protein), expressed from Addgene plasmid #61603, 1:100 (IHC & ICC)
LOX, Abcam #ab174316, 1:200 (IHC)
NF-κB1, Abcam #ab32360, 1:200 (IHC)
Fibronectin, Abcam #ab2413, rabbit, 1:100 (IHC)
Laminin, Novus #NB300-144, rabbit, 1:100 (IHC)
Denatured collagen (Cy3-CHP), 3Helix R-CHP #RED300, 1:10 (IHC)
Hyaluronan (Biotin-HABP), Amsbio #AMS.HKD-BC41, 1:100 (IHC)
α-SMA (1A4), Invitrogen #14-9760-82, mouse, 1:200 (ICC)
Paxillin, Abcam #ab32084, 1:200 (ICC)
α5 integrin, Abcam #ab25251, 1:200 (ICC)
p53, Abcam #ab26, 1:200 (ICC)
TIMP3, Abcam #ab39184, 1:200 (ICC)
YAP1, Cell Signaling Technology #14074, 1:200 (ICC)
Anti-mouse IgG, Abcam #ab6668, 1:100 (IHC and ICC involving mouse primary antibodies)
Collagen I (3G3), Santa Cruz #sc-293182, 1:100 (Immunogold labeling)
Goat anti-rabbit IgG (H+L) CF Biotium #20043, 1:1000 (IHC & ICC)
Goat anti-mouse IgG (H+L) CF Biotium #20040, 1:1000 (ICC)
Goat anti-rat IgG (H+L) CF Biotium #20283, 1:1000 (ICC)
Goat anti-mouse IgG (H+L) Alexa Fluor™ 488-10 nm colloidal gold, Invitrogen A-31561, 0.3 ug/mL (Immunogold SEM)
F-actin (CF Phalloidin), Biotium #00044, 1:500 (IHC & ICC)
Nucleus (Hoescht 33342), Invitrogen #H3570 (IHC & ICC)

Validation

The antibodies/binding proteins used in this study have been validated by the manufacturers or previous studies by the research group that developed the antibody/binding protein. All antibodies/binding proteins used have been widely used in other published works by many research groups for comparable sample types and applications.

Fibronectin, product website (https://www.abcam.com/products/primary-antibodies/fibronectin-antibody-ab2413.html)
Laminin, product website (https://www.novusbio.com/products/laminin-antibody_nb300-144)
Hyaluronan binding protein, product website (https://www.amsbio.com/biotinylated-hyaluronan-binding-protein-b-habp-versican-g1-domain-vg1-amshkd-bc41)
COL1A1 (3G3), product website (https://www.scbt.com/p/col1a1-antibody-3g3)
Cy3-collagen hybridizing peptide, developed by Dr. S Michael Yu's group at Johns Hopkins University (Targeting collagen strands by photo-triggered triple-helix hybridization. Proc. Natl. Acad. Sci. U.S.A., 2012; Targeting and mimicking collagens via triple helical peptide assemblies. Curr. Opin. Chem. Biol., 2013)
α-SMA, product website (https://www.thermofisher.com/antibody/product/Alpha-Smooth-Muscle-Actin-Antibody-clone-1A4-Monoclonal/14-9760-82)
YAP1, product website (https://www.cellsignal.com/products/primary-antibodies/yap-d8h1x-xp-rabbit-mab/14074?_requestid=1798067)
α5 integrin, product website (https://www.abcam.com/en-us/products/primary-antibodies/integrin-alpha-5-antibody-5h10-27-mfr5-ab25251)
TIMP3, product website (https://www.abcam.com/en-us/products/primary-antibodies/timp3-antibody-ab39184#application=icc-if)
LOX, product website (https://www.abcam.com/en-us/products/primary-antibodies/lox-antibody-epr4025-ab174316)
NF-κB1, product website (https://www.abcam.com/en-us/products/primary-antibodies/nfkb-p105-p50-antibody-e381-ab32360)
Paxillin, product website (https://www.abcam.com/products/primary-antibodies/paxillin-antibody-y113-ab32084.html)
CNA35 collagen binding protein, developed by Dr. Maarten Merkx's group at Eindhoven University of Technology (Fluorescently labeled collagen binding proteins allow specific visualization of collagen in tissues and live cell culture. Anal Biochem, 2006; Colorful Protein-Based Fluorescent Probes for Collagen Imaging. Plos One, 2014)
Goat anti-rabbit IgG, product website (https://biotium.com/product/goat-anti-rabbit-igg-hl/)
Goat anti-mouse IgG, product website (https://biotium.com/product/goat-anti-mouse-igg-hl/)
Goat anti-rat IgG, product website (https://biotium.com/product/goat-anti-rat-igghl-highly-cross-adsorbed/)

Goat anti-mouse IgG-10nm colloidal gold, product website (https://www.thermofisher.com/antibody/product/Goat-anti-Mouse-IgG-H-L-Secondary-Antibody-Polyclonal/A-31561)
Phalloidin, product website (https://biotium.com/product/phalloidin-conjugate/)
Hoescht 33342, product website (https://www.thermofisher.com/order/catalog/product/H3570)

Animals and other research organisms

Policy information about studies involving animals; ARRIVE guidelines recommended for reporting animal research, and Sex and Gender in Research

Laboratory animals	Mice are housed in individually ventilated cages with sex-matched littermates, 12 hours light-dark cycles, ambient temperature (20-24 degrees C) and humidity (30%-70%), and ad-libitum food and water supply. For DECIPHER sample preparations, C57BL/6J, young (4-8 weeks) or old (18-24 months) female mice were used. For mass spectrometry experiments, C57BL/6J, young (4 weeks) or old (24 months) female mice were used. For primary cell isolation, C57BL/6J, young (4 weeks) or old (24 months) female mice were used, with regularly confirmed negative mycoplasma contamination in subsequent experiments.
Wild animals	No wild animals were used in this study.
Reporting on sex	All mice used were female.
Field-collected samples	No field-collected samples were used in this study.
Ethics oversight	The use of mice in this study was approved by Institutional Animal Care and Use Committee (IACUC protocol R22-0579) and Tissue Sharing Programme under IACUC, National University of Singapore, and carried out in compliance with relevant guidelines and regulations.

Note that full information on the approval of the study protocol must also be provided in the manuscript.